

Estimation of Regional-Scale Near Real Time Reference Evapotranspiration Using Remote Sensing and Weather Data to Improve Agriculture Advisory

Anil Kumar Soni (✉ anilsonimnnit@gmail.com)

University of Allahabad

Jayant Nath Tripathi

University of Allahabad

Kripan Ghosh

India Meteorological Department

Priyanka Singh

India Meteorological Department

M. Sateesh

King Abdullah University of Science and Technology

K. K. Singh

India Meteorological Department

Research Article

Keywords: Evapotranspiration, FAO-56 Penman-Monteith, INSAT 3D, GFS-T1534, Insolation, GLDAS

Posted Date: July 11th, 2023

DOI: <https://doi.org/10.21203/rs.3.rs-3130231/v1>

License:  This work is licensed under a Creative Commons Attribution 4.0 International License.

[Read Full License](#)

Additional Declarations: No competing interests reported.

Version of Record: A version of this preprint was published at Earth Science Informatics on December 20th, 2023. See the published version at <https://doi.org/10.1007/s12145-023-01197-z>.

Abstract

Accurate and timely information of evapotranspiration (ET_0) is essential for multiple agricultural applications, including irrigation scheduling, studying crop-specific water loss at different growth stages, predicting crop yields, and forecasting drought conditions. The aim of this study is to examine the spatiotemporal patterns of ET_0 and facilitate the monitoring of crop water demand, optimizing irrigation water usage, and enhancing agricultural advisory services. This paper estimates regional-level daily ET_0 gridded data with a spatial resolution of 12.5 km by integrating observed weather data, IMD GFS-T1534 reanalysis data, and INSAT-3D satellite-based insolation product using the standard FAO56 Penman-Monteith empirical equation. The estimated monthly mean of ET_0 across India ranged from 10 to 400 mm. ET_0 exhibited an increasing trend from January to May, reaching its maximum values in May. In June, ET_0 significantly decreased as the monsoon arrived, coinciding with the movement of rainfall patterns. The month of December exhibited the lowest ET_0 values. The estimated daily gridded ET_0 was compared with station-based ET_0 , resulting in daily correlation coefficient R^2 and daily maximum absolute percentage errors ranging from 0.34 to 0.90 and 10% to 27% respectively. However, these errors decreased to a large extent when considering multiday accumulated values. A comparison was conducted between the GLDAS model ET_0 and the station-estimated values, revealing an overestimation of ET_0 by the GLDAS model. Additionally, significant variations were observed among the meteorological subdivisions. This highlights the necessity for proper calibration of the GLDAS model ET_0 or its effective agricultural application.

1. Introduction

Agriculture holds significant importance in driving the socio-economic growth of developing countries such as India, serving as the primary source of livelihood for a substantial portion of the population. As per the 2011 Census, the agricultural and allied sector activities engage 54.6% of the total workforce (Annual Report 2020-21, 2021). Adequate water availability at the right time is crucial for agriculture as it directly influences crop yields. However, the impact of climate change has resulted in irregular precipitation patterns (Soni et al., 2023a), leading to adverse effects on agricultural productivity in the country (Abeysekara et al., 2023; Jha et al., 2023; Ondrasek, 2014; Zhang et al., 2023; Zizinga et al., 2022). Various meteorological and agriculture departments actively engage in providing agricultural advisories to farmers. Among these advisories, information on when to irrigate and how much to irrigate holds great significance for farmers (Cahn and Johnson, 2017; Lorite et al., 2012). It not only helps farmers to save money and enhance crop productivity but also reduces excessive water usage in irrigation.

Evapotranspiration (ET) plays a significant role in soil water balance models and various crop water requirement-based models, following precipitation. These models are instrumental in obtaining accurate estimates for irrigation scheduling (Zhang et al., 2011), optimizing irrigation practices, understanding crop water requirements, and predicting yields (Attia et al., 2022; Chen et al., 2023; Lee et al., 2022; Wu et al., 2022). The availability of daily or weekly ET data, along with current soil moisture conditions and

weather forecasts, is invaluable in accurately determining crop water requirements and helpful in providing timely irrigation advisories. This integrated approach enhances the effectiveness of water resource management and aids in optimizing agricultural practices (Vuolo et al., 2015).

Evapotranspiration (ET) encompasses the combined water loss from the Earth's surface through soil evaporation and plant transpiration (Allen et al., 1998a; Kite, 2000). Evapotranspiration (ET) includes various terms, namely potential evapotranspiration (PET), reference evapotranspiration (ET_0), and actual evapotranspiration (AET). PET represents the maximum amount of water that could evaporate and be transpired under optimal conditions, assuming an adequate water supply without considering soil moisture constraints. ET_0 serves as a benchmark, representing the evaporative demand for a reference crop, such as well-watered grass, considering sufficient water availability. It helps estimate crop water requirements in diverse regions and crops. On the other hand, AET refers to the measured or estimated water loss (evaporation and transpiration) specific to a particular crop. AET can be derived from ET_0 by multiplying with the crop coefficient (k_c) (Allen et al., 1998b; Pereira et al., 1999).

The estimation of evapotranspiration relies on various techniques that utilizes meteorological and satellite data inputs. Several empirical equations have been developed to estimate evapotranspiration; however, these methods have limitations in terms of data availability and adaptability at the local scale (George H. Hargreaves and Zohrab A. Samani, 1985; Priestley and Taylor, 1972; Thornthwaite, 1948; Zhang et al., 2008). Empirical method Penman may require the wind calibration (Malek, 1994), radiation method performs good in humid conditions where aerodynamic influence contribution is comparatively small (Tabari et al., 2013; Vishwakarma et al., 2022) and temperature based empirical methods required local calibration (Lee, 2010). These empirical methods are suitable to estimate the water demand at low spatial resolution and monthly time scale. Among the available methods FAO-56 Penman Monteith (PM) empirical method estimates evapotranspiration relatively accurate and performs consistently for arid, semi-arid, and humid conditions at global scale (Abdollahnejad et al., 2018; Allen et al., 1998a; Subedi and Chávez, 2015) as it includes both thermodynamics and aerodynamic aspects. FAO 56 Penman Monteith, a globally accepted empirical equation for estimating evapotranspiration, requires multiple inputs such as air temperature, solar radiation, wind speed, and relative humidity. However, these inputs are often scarce and rarely available across space, making it challenging to accurately estimate water demand. In the developing countries like India, most of the studies have predominantly focused on the point scale due to limited weather station coverage and inconsistent data, which are insufficient for capturing precise spatial variability and translate this information in agriculture advisories. Choudhury, 1997 estimated the monthly global PET from the satellite data in which satellite derived solar radiation, fractional cloud cover, air temperature, and vapour pressure were used. Polar and geostationary satellite derived near surface air temperature and insolation were used to estimate PET estimation in most of the studies (Bois et al., 2008; Cruz-Blanco et al., 2014). Baik and Choi, 2015 estimated geostationary satellite-based Priestley-Taylor PET which was compared with high quality, global land surface model GLDAS (25 km) based PET and found significantly overestimated. Rao et al., 2012, estimated station-based PET for 51 stations using 8 different empirical methods and found that modified Penman Monteith

overestimated mostly during summer and Hargreaves method performed better during the northeast monsoon season compare to other three seasons. Over the past three decades, numerous researchers have dedicated their efforts to estimating evapotranspiration using various approaches such as satellite data, meteorological data, or a combination of both (Bhattarai et al., 2016; Huerta et al., 2022; S. Ha et al., 2020; Singer et al., 2021; Vyas et al., 2016; Zhang et al., 2016). However, despite these advancements, the full utilization of these methods and datasets is hindered by several challenges. One of the main hurdles is the scarcity of calibration and validation of datasets, which affects the accuracy and reliability of the estimations.

Evapotranspiration estimation is significantly influenced by solar radiation, as it is directly proportional to it. Even small uncertainties in solar radiation measurements can introduce considerable errors in evapotranspiration estimation (Heck et al., 2020). However, due to limitations in the availability and consistency of solar radiation data, an alternative solution for estimating evapotranspiration can be found in satellite-derived high spatial and temporal remote-sensed meteorological data. To address the uncertainties in solar radiation, this study developed and discussed a data integration approach that combines remotely sensed insolation product with observed daily meteorological data. This integration enables the estimation of near real-time evapotranspiration at a spatial resolution of 12.5 km and a daily temporal scale for the entire country of India. Although models such as the Global Land Data Assimilation System (GLDAS) also provide daily evapotranspiration estimates, these models tend to overestimate evapotranspiration and cannot be directly used without a proper calibration and validation at the regional scale. This paper focuses on the discussion and validation of the estimated regional evapotranspiration (ET_0) specifically in the context of its application in agriculture advisory services. The paper is organized as follows: section 2 (Methods and Materials), the paper comprehensively addressed the various components of the study. This encompassed discussions about the station observational data covering the 34 meteorological sub-divisions, the INSAT 3D insolation product, the gridded observed temperature product, and the GLDAS-based evapotranspiration. Moreover, the paper also provided insights into the process of deriving the estimated evapotranspiration, outlined the statistical methods utilized for error computation, and described the calibration procedure employed for result comparison. Section 3 (Results and Discussion) focused on the patterns of monthly evapotranspiration throughout the region, scrutinizing its 3 days to monthly and sub-divisional variations. The calibration coefficients for both proposed derived ET_0 and GLDAS model-based ET_0 were presented, alongside statistical comparisons, accuracy assessments, and an exploration of the daily temporal variation at the sub-division level. Finally, in the Summary and Conclusion section, paper discussed the potential use of satellite data in enhancing the quality of agriculture advisories in India and improving various models through the utilization of calibrated proposed evapotranspiration.

2. Material and methods

2.1 Study Area

This study primarily centres on the Indian subcontinent, encompassing a geographical range of latitude 7.5° to 37.5° N and longitude 67.5° to 97.5° E. The vast size and diverse topography of India contribute to its remarkably varied climate. The agricultural sector and water resources in India greatly rely on the southwest monsoon season. This period holds significant importance as certain regions receive as much as 75% of their annual rainfall during this time, making it a crucial determinant of the country's overall annual precipitation where annual rainfall ranges from 1100 mm to 2000 mm per year and distribution of rainfall over land mass varies widely. From 1901–2020 the monthly mean of average temperature varies between 18° C to 29° C with annual mean average 24° C.

The climate of India can be categorized into different regions, including tropical, subtropical, and arid/semi-arid regions. The tropical regions are predominantly located in the southern and eastern parts of the country and are characterized by consistently high temperatures throughout the year. Subtropical regions, located in the northern and central parts of India, experience seasonal variations in temperature with hot summers and cold winters. These regions receive rainfall primarily during the monsoon season, although in lesser amounts compared to the tropical regions. Arid or semi-arid regions are primarily situated in the northwest and western parts of India. These regions face low and erratic rainfall throughout the year, resulting in drought conditions and water scarcity (Rajeevan and Nayak, 2017; Soni et al., 2023). India is divided into 36 meteorological subdivisions based on the unique rainfall patterns observed across the country (Fig. 1).

2.2 Data

2.2.1 Observed station data

In this study, we selected 34 Agrometeorological observatories (Table 1) to ensure representation from each meteorological subdivision (Fig. 1). This strategic selection facilitated effective validation and calibration of the estimated evapotranspiration (ET_0). The Agromet observatories are equipped with sensors to measure various weather variables including maximum and minimum temperature, maximum and minimum relative humidity, rainfall, bright sunshine hours, and evaporation. These stations cover a wide range of conditions, including rainfed and irrigated areas, diverse weather patterns, topography, and soil types. Consequently, the impact of weather and other physical variables was thoroughly investigated. Ground observations from agricultural fields were collected for the years 2017 and 2018.

Table 1
Details of IMD Agromet observatories and data used

Sl. No.	ID	Station	Sub Division	Lat	Long	Alt (m)
1	42213	Basar	Arunachal Pradesh	27.98	94.66	578
2	42428	Sonitpur	Assam and Meghalaya	26.72	93.14	84
3	42501	Sabour	Bihar	25.24	87.04	41
4	42785	Korba	Chattishgarh	22.5	82.55	325
5	43178	Guntur Lam	Coastal AP	16.36	80.42	31
6	43288	Vittal	Coastal Karnataka	12.76	75.03	70
7	42677	Jabalpur	East MP	23.81	79.96	422
8	42344	Durgapura	East Rajasthan	26.85	75.78	401
9	42363	Lucknow	East UP	26.84	80.94	117
10	42814	Kalyani	Gangetic WB	22.97	88.43	16
11	42537	Dantiwada	Gujarat Region	24.32	72.31	172
12	42133	Karnal	Haryana	29.68	76.99	252
13	42082	Solan	Himachal Pradesh	30.85	77.16	1241
14	42070	Kandi	Jammu & Kashmir	32.38	75.69	458
15	42702	Ranchi	Jharkhand	23.39	85.31	655
16	43398	Vellanikara	Kerala	10.54	76.27	35
17	13	Roha	Konkan and Goa	18.43	73.11	11
18	42919	Kundewadi	Madya Maharastra	20.09	74.07	554
19	43016	Parbhani	Marathwada	19.26	76.77	417
20	43190	Raichur	N.I.Karnataka	16.21	77.34	393
21	42528	Jharnapani	NMMT	25.75	93.84	304
22	42896	Ranital	Odisha	21.15	86.54	20
23	42128	Faridkot	Punjab	30.59	74.82	207
24	43238	Anantpur	Rayalaseema	14.69	77.66	349
25	43269	Navile(A)	S.I. Karnataka	13.09	76.44	862
26	42508	Gossaigaon	SHWB	26.43	89.97	51
27	42833	Junagadh	Sourashtra	21.52	70.45	90

Sl. No.	ID	Station	Sub Division	Lat	Long	Alt (m)
28	43384	Kovilpatti	Tamilnadu	9.16	77.87	110
29	43131	ICRISAT	Telangana	17.51	78.27	552
30	42150	Pantnagar	Uttarakhand	29.02	79.48	234
31	42936	Akola	Vidarbha	20.7	77	292
32	42461	Datia	West MP	25.68	78.56	218
33	42162	Bikaner	West Rajasthan	28.08	73.36	226
34	42142	Nagina	West UP	29.44	78.43	252

2.2.2 IMD gridded temperature data

Temperature is a critical parameter in the estimation of evapotranspiration, and the use of an accurate data is of utmost importance. In this study, we utilized gridded maximum and minimum temperature data obtained from the National Climate Centre (NCC) of the India Meteorological Department (IMD) (<https://www.imdpune.gov.in/lrfindex.php>, accessed on August 24th, 2021). This dataset is available at a daily frequency with a spatial resolution of $0.5^\circ \times 0.5^\circ$ (approximately 2500 km^2). It has been found to be highly reliable compared to other datasets available for the Indian region, exhibiting an error of less than 0.5°C during cross-validation. Moreover, this dataset successfully captures the mean frequency of cold and heat waves, as well as temperature anomalies associated with monsoon breaks (Srivastava et al., 2009).

2.2.3 SRTM DEM data

SRTM (Shuttle Radar Topography Mission) DEM (Digital Elevation Model) data provides elevation information for nearly the entire Earth's surface, covering approximately 80% of the globe. It is a joint collaboration between National Aeronautic Space Administration (NASA), National Geospatial Intelligence Agency (NGA), and the German Aerospace Center (DLR). It has been widely used in various applications such as geology, hydrology, cartography, and terrain analysis. In this study, we utilized SRTM 90m (3 Arc second) spatial resolution DEM data (Version 4). This dataset can be accessed through platforms like the United States Geological Survey (USGS), NASA's Earthdata Search, and the CGIAR-CSI SRTM 90m Database (<https://srtm.csi.cgiar.org/> accessed on 28th August 2021). SRTM radar used C and X band for the preparation of DEM data which has been further processed to fill data voids. (Jarvis et al., 2008).

2.2.4 Satellite derived insolation data

INSAT 3D (Indian Geostationary satellite) insolation product, 3DIMG_L2C_INS, provides data with a spatial resolution of 4 km and a temporal resolution of 30 min over the Asia Mercator region. This region spans from 44.5°E to 105.5°E longitude and 10.0°S to 45.5°N latitude. Insolation refers to the total amount of solar radiation flux or irradiance in the shortwave range of 0.3 to 3 μm , which reaches the

ground and consists of a combination of direct and diffuse components of solar radiation fluxes. In the retrieval of insolation data from INSAT 3D, two approaches are primarily utilized: statistical or empirical methods (Tarpyley, 1979) and physical or radiative transfer methods (Tanahashi et al., 2001). These approaches estimate surface insolation by making use of visible and thermal bands. The estimation of instantaneous and daily insolation is achieved through the implementation of a spectrally integrated irradiance model and a three-layer cloudy model, using the INSAT 3D visible (VIS), water vapor (WV), and thermal infrared (IR) bands (Bhattacharya et al., 2013). A trapezoidal integration was applied to construct the daily value from the instantaneous global irradiances in MJm^{-2} . The INSAT 3D insolation product exhibits significantly higher accuracy compared to other available products, such as Heliosat SARAH-E and the NASA MERRA-2 reanalysis product, with improvements of approximately 42.5% and 43.8% respectively (Kamath and Srinivasan, 2020).

2.2.5 Weather forecast model GFS T1534 reanalysis products

IMD runs weather forecast model GFS T1534 twice daily (00 and 12 UTC) on a horizontal spatial scale of 12.5 km and on a vertical scale of 64 hybrid sigma-pressure layers with a top layer centred around 0.27 hPa (~ 55 km) to generate 10 days' deterministic forecast in advance on MIHIR HPCS (Sridevi et al., 2020). Model gives the post processed output parameters at 25 km and 12.5 km spatial resolution. The atmospheric forecast model used in GFS is a global spectral model (GSM) with spherical harmonic functions. The IMD GFS T1534 operational model's dynamical core is based on two-time level semi-implicit Lagrangian discretization with three dimensional Hermite interpolation (Sela, 2010). The initial conditions are prepared at BHASKARA HPCS, NCMRWF to run the IMD-GFS model using NCEP Ensemble Kalman Filter (EnKF) based hybrid Global Data Assimilation System (GDAS) (Buehner et al., 2013). The model is based on the usual expressions of conservation of mass, momentum, and energy at T1534 spectral truncation 12.5 km physics gaussian grid and 64 levels in a hybrid sigma-pressure vertical grid (Kumar et al., 2019). The detailed structure and physics of Global Forecast System (GFS) are available at <http://www.emc.ncep.noaa.gov/GFS/doc.php>.

2.2.6 Global Land Data Assimilation System (GLDAS)

GLDAS model integrates the satellite and ground-based information using advanced land surface modelling and data assimilation techniques to produce the optimal field of land surface states and fluxes (Rodell et al., 2004). The reanalysed datasets through common land model (CLM), variable infiltration capacity model (VIC), and Noah LSM are available at GLDAS websites (<http://ldas.gsfc.nasa.gov/gldas/>) at various spatial scale (0.25° and 1°) and temporal scale (3 hr and monthly). In this study the GLDAS 0.25° (GLDAS_NOAH025_3H 2.1) has been used.

2.3 Methodology

The FAO-56 Penman-Monteith empirical method is widely employed for accurately estimating reference evapotranspiration (ET_0). However, this method necessitates a significant number of weather inputs,

including radiation, relative humidity, air temperature, wind speed, and vapor pressure. Unfortunately, these inputs are often not readily available at a suitable spatial and temporal scale in standard weather observatories. To address this issue of data scarcity from ground stations, we utilized a derived insolation product from the geostationary satellite INSAT-3D to estimate net radiation. Additionally, we incorporated observed India Meteorological Department (IMD) gridded temperature data, IMD GFS model based reanalysed data for relative humidity and wind speed, and SRTM DEM elevation data. The inclusion of observed and analysed inputs in the model yielded comparatively more accurate results in comparison to utilizing a general model for estimating ET_0 .

2.3.1 FAO-56 Penman-Monteith empirical reference ET_0 framework

In 1948, Penman developed an empirical equation to estimate evaporation from an open water surface (Penman, 1948). This equation takes into account meteorological parameters such as sunshine, temperature, humidity, and wind speed, utilizing an approach based on energy balance and mass transfer (see Fig. 2 and Table 2). Subsequently, this method was expanded to include cropped surfaces by incorporating factors such as aerodynamic resistance and surface resistance. The FAO proposed a standard parameterization of Penman-Monteith empirical method (Monteith, 1981) for estimation of daily grass reference evapotranspiration (ET_0) from a well-irrigated, homogenous, 0.12 m grass crop height, a fixed surface resistance of 70 s m⁻¹, and an albedo of 0.23 (Allen et al., 1998a). This empirical method, hereafter referred as PM, is a standard worldwide acceptable method to compute the daily reference ET_0 in mm and calculated as follows:

$$ET_0 = \frac{0.408\Delta(R_n - G) + \gamma \frac{900}{T+273} u_2(e_s - e_a)}{\Delta + \gamma(1 + 0.34u_2)}$$

1

where ET_0 is the grass-reference evapotranspiration in mm day⁻¹, R_n is net solar radiance at crop surface in MJ m⁻² day⁻¹, G is solar heat flux density in MJ m⁻² day⁻¹, T is air temperature at 2 m height in °C, u_2 is the wind speed at 2 m height in m s⁻¹, e_s is saturation vapour pressure in kPa, e_a is actual vapour pressure in kPa, $(e_s - e_a)$ is saturation vapour pressure deficit in kPa, Δ is slope vapour pressure curve in kPa °C⁻¹, γ is psychrometric constant equivalent to 0.665×10^{-3} P in kPa °C⁻¹.

Saturation vapour pressure $e^o(T)$ kPa at temperature T °C is computed using below empirical equation

$$e^o(T) = 0.6108 \exp \left[\frac{17.27T}{T + 237.3} \right]$$

2

Due to the non-linearity of the Eq. 2, the mean saturation vapour pressure for a day should be computed as the mean between the saturation vapour pressure at the mean daily maximum and minimum air temperature for that period.

$$e_s = \frac{e^o(T_{max}) + e^o(T_{min})}{2}$$

3

Actual vapour pressure (e_a) computed from the relative humidity and saturation vapour pressure using below empirical equation

$$e_a = \frac{e^o(T_{min}) * \frac{RH_{max}}{100} + e^o(T_{max}) * \frac{RH_{min}}{100}}{2}$$

4

The slope vapour pressure curve (Δ) [kPa °C-1] at given air temperature $T^\circ\text{C}$ is computed by

$$\Delta = \frac{4098 \left[0.6108 \exp \left(\frac{17.27T}{T+237.3} \right) \right]}{(T + 237.2)^2}$$

5

The psychrometric constant (γ) is computed using P daily mean atmospheric pressure (kPa), λ the latent heat of vaporization (2.45 MJ kg^{-1}), C_p the specific heat at constant pressure ($1.013 \times 10^{-3} \text{ MJ kg}^{-1} \text{ }^\circ\text{C}^{-1}$), ϵ ratio molecular weight of water vapor/ dry air (0.622) given by

$$\gamma = \frac{C_p P}{\epsilon \lambda} = 0.000665 P$$

6

where mean atmospheric pressure P (kPa) can be computed from the elevation in meters z by using below equation

$$P = 101.3 \left(\frac{293 - 0.0065z}{293} \right)^{5.26}$$

7

Wind speed at 2 m height is required to compute ET_0 . Generally, in meteorology operations anemometers are placed at 10 m height and in agrometeorology it is placed on the 2 m or 3 m height. To adjust the wind speed data a logarithmic wind speed profile is used for measurement above a short-grassed surface

$$u_2 = u_z \frac{4.87}{\ln(67.8z - 5.42)}$$

8

The soil heat flux (G) is the energy that is used in heating the soil. Positive value of G shows that soil is warming and negative value of G shows the soil is cooling. In estimation of ET_0 , soil heat flux is negligible compared to R_n when surface is fully covered with vegetation

$$G \approx 0$$

9

Net solar radiation ($\text{MJ m}^{-2} \text{ day}^{-1}$) is the difference of net shortwave solar radiation and net longwave solar radiation.

$$R_n = R_{netshortwave} - R_{netlongwave}$$

10

$$R_{netshortwave} = (1 - \alpha) R_{Surfaceinsolation}$$

11

where α is albedo of a hypothetical grass reference crop with the value of 0.23 (Allen et al., 1998a).

The earth absorbed the solar radiation and convert it to heat energy. Some of the longwave radiation is absorbed by the atmosphere and some of loses into space. Net longwave solar radiation (R_{nl}) is computed using the empirical equation

$$R_{nl} = \sigma \left[\frac{T_{max,k}^4 + T_{min,k}^4}{2} \right] (0.34 - 0.14\sqrt{e_a}) \left(1.35 \frac{R_s}{R_{so}} - 0.35 \right)$$

12

where R_{nl} is net outgoing longwave radiation ($\text{MJ m}^{-2} \text{ day}^{-1}$), σ is Stefan-Boltzmann constant ($4.903 \times 10^{-9} \text{ MJ K}^{-2} \text{ m}^{-2} \text{ day}^{-1}$), $T_{max,k}$ is maximum absolute temperature during 24 hr period in Kelvin, $T_{min,k}$ is minimum absolute temperature during 24 hr period in Kelvin, e_a is actual vapour pressure (kPa), R_s is solar radiation ($\text{MJ m}^{-2} \text{ day}^{-1}$), R_{so} is clear sky radiation ($\text{MJ m}^{-2} \text{ day}^{-1}$), and R_s/R_{so} is relative shortwave radiation (limited to ≤ 1.0).

Clear sky radiation can be computed

$$R_{so} = (0.75 + 2 \times 10^{-5} Z) R_a$$

13

where Z is the station elevation above sea level (m) and R_a is the extraterrestrial radiation ($\text{MJ m}^{-2} \text{ day}^{-1}$).

The extraterrestrial radiation can be computed

$$R_a = \frac{24(60)}{\pi} G_{sc} d_r [\omega_s \sin(\varphi) \sin(\delta) + \cos(\varphi) \cos(\delta) \sin(\omega_s)]$$

14

where R_a is extraterrestrial radiation ($\text{MJ m}^{-2} \text{ day}^{-1}$), G_{sc} is solar constant equal to $0.0820 \text{ MJ m}^{-2} \text{ min}^{-1}$, d_r is inverse relative distance between Earth and Sun, ω_s is sunset hour angle in radian, ϕ is latitude in radian, δ is solar decimation in radian.

$$d_r = 1 + 0.033 \cos\left(\frac{2\pi J}{365}\right)$$

15

$$\delta = 0.409 \sin\left(\frac{2\pi J}{365} - 1.39\right)$$

16

where d_r is inverse distance between earth and sun, δ is solar decimation angle, J is number of days between 1 to 365 or 366 in Julian date.

$$\omega_s = \arccos(-\tan(\varphi) \tan(\delta))$$

17

where ω_s is sunset hour angle and range between -1 to 1.

Day light hours calculated from the sunset angle in radians

$$N = \frac{24\omega_s}{\pi}$$

18

Solar radiation is derived from the station measured bright sunshine hours (BSSH) and day light hours (N) using empirical equation.

$$\text{Solar Radiation} = a + \left(\frac{b * \text{BSSH}}{N} \right) * R_a$$

where $a = 0.25$ and $b = 0.5$ are constants, R_a is extraterrestrial radiation and N is day light hours.

Table 2
Data used

S. No.	Data	Spatial Resolution	Temporal resolution	Data Latency
1	IMD Gridded Temperature (Tmax and Tmin)	0.5° x 0.5°	daily	1 Day
2	INSAT 3D Insolation	0.04° x 0.04°	Daily	1 Day
3	GFS T1534 reanalysed Wind	0.125° x 0.125°	Daily	1 Day
4	GFS T1534 reanalysed Relative Humidity	0.125° x 0.125°	Daily	1 Day
5	SRTM DEM	90 m	NA	NA

2.3.2 Statistical analysis used for error estimation

A statistical analysis was conducted to compare the estimates from weather stations with the estimated gridded reference evapotranspiration (ET_0) data. Evaluation metrics such as mean absolute percentage error (MAPE), root mean square error (RMSE), coefficient of determination (R^2), and Nash-Sutcliffe Efficiency (NSE) were calculated at both daily and monthly temporal scales.

2.3.2.1 Mean Absolute Percentage Error (MAPE)

MAPE is a measure of prediction accuracy in percentage of predicted (P) with respect to observed data (O). It is calculated using the below empirical equation

$$MAPE = \frac{\sum_{i=1}^n \left| \frac{O_i - P_i}{O_i} \right|}{n} \times 100$$

2.3.2.2 Coefficient of determination (R^2)

Coefficient of determination (R-squared) is basically “goodness of fit” and is the proportion of the fluctuations in the dependent variable that is predictable from the independent variable. R^2 values varies between 0 to 1, where 1 represents a perfect fit and 0 represents that the model fails.

$$R^2 = \left[\frac{\sum_{i=1}^n (O_i - \bar{O})(P_i - \bar{P})}{\sqrt{\sum_{i=1}^n (O_i - \bar{O})^2} \sqrt{\sum_{i=1}^n (P_i - \bar{P})^2}} \right]^2$$

21

where O_i is daily observed ET_0 and P_i is daily estimated gridded ET_0 .

2.3.2.3 Nash-Sutcliffe efficiency coefficient (NSE)

The Nash-Sutcliffe efficiency (*NSE*) is a normalized statistic that determines the relative magnitude of the residual variance (“noise”) compared to the measured data variance (“information”) (Nash and Sutcliffe, 1970). The *NSE* varies between 1 (perfect fit) to $-\infty$. The *NSE* less than 0 indicates that the mean value of observed time series data would have been a better predictor than the simulated model time series data.

$$NSE = 1 - \left[\frac{\sum_{i=1}^n (O_i - P_i)^2}{\sum_{i=1}^n (O_i - \bar{O})^2} \right]$$

22

where O_i is daily observed ET_0 and P_i is daily estimated gridded ET_0 .

2.3.3 Bias Correction

In this study, we utilized the simple and data-efficient linear bias correction statistical method. To accurately capture weather conditions and ET_0 , we computed a yearly scale factor (α) based on a time series of station-estimated ET_0 and gridded-estimated ET_0 data (Eq. 23). To overcome the limitations arising from limited data availability, we considered meteorological subdivisions, which group regions exhibiting similar weather patterns. For each subdivision, we determined a bias scale factor by leveraging ground station data. This approach effectively encompasses the wide spectrum of weather conditions and evapotranspiration patterns found across various subdivisions, despite the constraints posed by limited station data availability.

$$Scaling factor (\alpha) = \frac{mean_{observed}}{mean_{simulated}}$$

23

2.3.4 Probability of Detection (POD)

The performance diagram (Roebber, 2009) is a valuable tool for comparing the probability of detection (POD) and success ratio (SR) between two datasets: estimated gridded ET_0 and GLDAS model ET_0 . It utilizes a contingency table (Table 3) to assess hits, false alarms, misses, and missing rejections when comparing observed values to derived products. This diagram enables a comprehensive evaluation of these metrics, providing insights into the performance and agreement of the datasets. The comparison was conducted between the gridded estimated ET_0 , GLDAS ET_0 , and station-estimated ET_0 for the period 2017–2018. ET_0 values were categorized as low (0–5 mm), medium (5–10 mm), and high (10–15 mm), allowing for a thorough analysis of dataset performance within different ET_0 ranges.

$Probability of Detection (POD) = \frac{A}{A+C}$	(24)
$False Alarm Rate (FAR) = \frac{B}{A+B}$	(25)
$Success Ratio (SR) = 1 - FAR$	(26)

Table 3: Contingency table

2 X 2 Contingency Table		Event Observed	
		Yes	No
Event Forecast	Yes	A	B
	No	C	D

3. Results and discussions

3.1 Spatiotemporal distribution of ET_0 over the Indian region

Evapotranspiration varies throughout the year in response to seasonal changes, as it is influenced by factors such as radiation and temperature. Figure 3 illustrates the spatiotemporal variations of monthly ET_0 . From January to May, ET_0 gradually increases due to rising in surface temperatures. However, from June to September, ET_0 decreases as the southwest monsoon arrives and progresses. During October to December, ET_0 further decreases due to declining surface temperatures. Notably, in January and February, certain regions such as Gujarat, Rajasthan, Central Maharashtra, Karnataka, Telangana, West Andhra Pradesh, and Tamil Nadu exhibit comparatively high ET_0 values to other regions. These elevated ET_0 values during the Rabi season may necessitate field-level interventions for risk management, especially if they coincide with critical stages of Rabi crops like wheat.

March onwards until the onset of the monsoon, ET_0 rapidly increases over India, except in extreme north and northeast regions, due to the rise in temperature and solar radiation. As the monsoon arrives and progresses, ET_0 values decrease. However, in rainfed regions, where Kharif crops depend on rainfall, it is essential to regularly monitor water stress in plants to address the high evapotranspiration demand and provide timely irrigation. The regular monitoring of evapotranspiration under the present climate variability and erratic monsoon behaviour is crucial for effective climate risk management.

The North-eastern and Western Ghats region of India exhibited minimal annual variability in ET_0 values, primarily due to consistently low temperatures throughout the year. On the other hand, the North-western, central, and certain areas of the northern plains (Rajasthan, Gujarat, Madhya Pradesh, Bihar, and Uttar Pradesh) experienced the highest annual variability in ET_0 . The monthly sub-division wise heatmap (Fig. 4) clearly illustrates that these regions, including East and West Rajasthan, N. I. Karnataka, Coastal A. P., Tamil Nadu, Gujarat, Rayalaseema, Marathwada, and Madhya Pradesh, consistently show high ET_0 values throughout most months of the year. As these regions are predominantly rainfed and prone to drought (Soni et al., 2023b), accurate ET_0 values are crucial for planning appropriate crop types and cropping patterns to maximize agricultural productivity.

3.2 Daily temporal variation of ET_0 at meteorological subdivision level

Regions such as hilly and coastal areas exhibit relatively low temporal variation in ET_0 (Fig. 4), ranging from 0.8 mm to 6.5 mm. On the other hand, the northern plains, central and southern parts of India (excluding the coastal region) display high temporal variation, with values ranging from 0.8 mm to 12.14 mm throughout the year. These rainfed regions, characterized by significant variations in the southwest monsoon, are susceptible to drought, highlighting the need for timely information to assess and manage irrigation scheduling and other agricultural operations.

In the time series (Fig. 5), it is clear that the ET_0 is following the same pattern and temporal variation for year 2017 and 2018. Central and few areas of Northern plains of India (Rajasthan, Gujarat, Madhya Pradesh, Bihar and Uttar Pradesh) shows high standard deviation with variation 1.44 to 2.23 mm, North-eastern region shows low standard deviation with variation 0.9 to 1.0 mm, northern hilly region varies 1.26 to 1.85 mm, coastal region varies 0.8 to 1.68 mm, and south region except coastal varies 1.1 to 1.68 mm. Spatial analysis of ET_0 carried out (Rao et al., 2012) also reflects the low ET_0 value over hilly and coastal region whereas comparatively high values over arid regions and central India due to high advective energy and high atmospheric demand over the area.

3.3 Calibration of satellite based ET_0 estimates

The calibration and validation of estimated gridded ET_0 at the sub-divisional level provides greater confidence in the agricultural scientific community when issuing advisories to farmers and planners. A

linear bias correction method was employed to estimate bias correction factor (α) for the year 2017 and 2018. Figure 6 depicts that the bias factor remains relatively stable for both years, except in Himachal Pradesh where there was limited data available for the year 2018. In this study, the bias correction factor (α) was derived from the 2017 data and applied as a correction factor to the daily estimated gridded ET_0 for 2018. Different seasons are influenced by various parameters impacting ET_0 , as evidenced by the sensitivity analysis of the PM empirical equation (Bois et al., 2008). For example, wind speed exhibits the highest sensitivity during winters, while net solar radiation holds greater influence during the summer season. The study also suggests conducting seasonal calibration to minimize errors introduced by input parameters. The estimated gridded ET_0 generally tends to be overestimated across all meteorological subdivisions, but it exhibits a strong correlation with the station estimates. Figure 7 demonstrates a significant reduction (ranging from 60–80%) in MAPE error in subdivisions like Himachal Pradesh and Punjab, both at daily and monthly scales. The Nash-Sutcliffe Efficiency (NSE) statistics (Fig. 8) generally indicate values below 0.5, except for Chhattisgarh, Coastal AP, East MP, Kerala, Rayalaseema, and Sourashtra. However, after applying bias correction calibration, the ET_0 of 79% of the meteorological subdivisions showed improvement, with values exceeding 0.5.

3.4 Statistical comparison of estimated gridded ET_0 with station ET_0

Stations were carefully chosen to cover each and every meteorological subdivision, ensuring comprehensive coverage. The evaluation of the estimated gridded ET_0 performance was conducted at different temporal scales, ranging from daily to monthly, using statistical parameters such as R^2 , NSE, and MAPE. Substantial variations in the statistical parameters were observed among the meteorological subdivisions at the daily scale, but the accuracy significantly improved when comparing the datasets at higher temporal scales. The daily coefficient of correlation (R^2) values between the datasets of station estimates and nearest grid estimates of gridded ET_0 varied from 0.34 to 0.9. A notable improvement was observed at the 3-day accumulated temporal scale, where R^2 values ranged from 0.68 to 0.94. Subsequently, further improvement in accuracy was observed at higher temporal scales (Fig. 9). The Nash-Sutcliffe Efficiency (NSE) score, comparing station estimates and nearest grid estimates of gridded ET_0 , exhibited a similar trend (ranging from 0.16 to 0.88) to the coefficient of correlation (R^2), with a low NSE values in subdivisions such as Coastal Karnataka, S. I. Karnataka, and N.I. Karnataka (Fig. 10). Since NSE measures the relative accuracy of the model estimates compared to the average observed value, it is evident that accuracy improves with a higher temporal scale, highlighting the quantitative improvement in accuracy. The Maximum Absolute Percentage Error (MAPE) ranged from 10–27% at the daily scale, and a notable reduction in error was observed as the temporal scale increased (Fig. 11). High MAPE (>20%) values over the Arunachal Pradesh, Bihar, Concan and Goa, Gangetic WB, Haryana, Jammu and Kashmir, Punjab, SHWB, Uttarakhand, and West UP meteorological subdivisions and low MAPE (<15%) values over East MP, Kerala, Odisha, Rayalaseema, Sourashtra, Telangana, and West MP.

Coastal regions (Coastal Karnataka, Gangetic WB, Odisha, Kerala, Conkan & Goa, N. I. Karnataka, S. I. Karnataka, and Tamilnadu) and certain hilly regions (Arunachal Pradesh, Assam & Meghalaya, and NMMT) display higher MAPE errors and lower values of R^2 and NSE. These differences can primarily due to the uncertainty in wind data in coastal areas and temperature variations in hilly regions. Considering the inherent variations in daily ET_0 , its practicality in agriculture advisory may be somewhat limited when compared to the more reliable multiday accumulated ET_0 values. The multiday accumulated ET_0 values demonstrate a significant enhancement in accuracy and can be harnessed effectively for diverse agricultural planning purposes such as water budgeting, irrigation scheduling, and more.

3.5 Statistical comparison of GLDAS model ET_0 with station ET_0

The Global Land Data Assimilation System (GLDAS) provides a 3-hourly ET_0 product that can be accumulated over different time intervals, ranging from daily to monthly, for comparison with station-estimated ET_0 . When assessing ET_0 at a daily scale, the GLDAS model-based ET_0 exhibited satisfactory agreement in most of the meteorological subdivisions, with correlation coefficients ranging from 0.1 to 0.9 and NSE coefficient ranging from -1.3 to 0.8 (Fig. 12). Without calibration, the Mean Absolute Percentage Error (MAPE) varied from 74–233%, but after calibration, it decreased to a range of 12–52% (Fig. 13). In summary, it can be concluded that the GLDAS ET_0 tends to significantly overestimate values and, therefore, requires calibration before practical use.

The meteorological subdivisions of Arunachal Pradesh, Assam & Meghalaya, Coastal Karnataka, Gangetic WB, N. I. Karnataka, NMMT, Odisha, S. I. Karnataka, and SHWB displayed a weak correlation (R^2 less than 0.5) at the daily scale. Furthermore, there was no observed improvement in the North Eastern subdivisions of Arunachal Pradesh, NMMT, and SHWB even at the monthly time scale. The NSE score also indicated a poor relationship between the datasets in most of the subdivisions, with negative values observed for Arunachal Pradesh, Assam and Meghalaya, Coastal Karnataka, NMMT, Odisha, SHWB, and Tamil Nadu. Although some subdivisions like Tamil Nadu, Odisha, Jharkhand, Gangetic WB, and Assam and Meghalaya showed good agreement (R^2), the NSE score clearly indicates poor relative accuracy of the model estimates compared to the average observed value (Fig. 14 and Fig. 15).

3.6 Statistical comparison of GLDAS ET_0 with estimated gridded ET_0

GLDAS ET_0 estimates are valuable but they have certain limitations. The model relies on input data and have certain assumptions that may introduce uncertainties. Local calibration and validation are necessary to improve the accuracy in a specific region. As mentioned in the earlier section, it was observed that the GLDAS model overestimated ET_0 , indicating that the overall ET_0 values is reduced by approximately 54% after bias correction (Fig. 16). Season-wise analysis was conducted for both

calibrated estimated gridded ET_0 and calibrated GLDAS ET_0 . As shown in Fig. 17, the RMSE error was found to be higher during the Monsoon and pre-monsoon seasons across most subdivisions. In contrast, it was lower during the post-monsoon and winter seasons, which can be attributed to the lower temperatures and solar radiation during those periods. A similar pattern was observed in GLDAS ET_0 , although with a higher standard deviation and RMSE, as depicted in Fig. 18. In the winter and post-monsoon seasons, the estimated gridded ET_0 exhibits a low RMSE, with most stations recording values below 0.5 mm. Furthermore, there is a strong correlation agreement ranging from 0.6 to 0.9 among all stations, except for Jharkhand. However, in the case of GLDAS ET_0 , the RMSE values for most stations range from 0.4 to 1 mm, with a correlation agreement ranging from 0.2 to 0.9, except for Arunachal Pradesh, Jammu, and SHWB. During the pre-monsoon and monsoon seasons, the estimated gridded ET_0 shows an RMSE ranging from 0.5 to 1 mm, with approximately 80% of stations displaying a correlation greater than 0.6. On the other hand, GLDAS ET_0 exhibits an RMSE ranging from 0.5 to 1.5 mm, with around 60% of stations having a correlation greater than 0.6. The accuracy of both datasets is relatively lower during the monsoon season, and they demonstrate similar behaviour to the pre-monsoon period. The findings of the study indicate that GLDAS ET_0 can be reliably utilized during the post-monsoon and winter seasons. However, for the pre-monsoon and monsoon seasons, further investigation and calibration of the GLDAS model ET_0 are recommended to enhance its accuracy in those periods.

3.7 Probability of detection (POD)

The estimated gridded ET₀ and GLDAS ET_0 were compared to ground observations for the period 2017–2018. The datasets were divided into three categories based on ET_0 values: low (0–5 mm), medium (5–10 mm), and high (10–15 mm). In Figure-19, the performance of the two datasets is represented by POD and SR scores for the low (red) and medium range ET_0 (black) categories, which show good agreement. However, the performance of GLDAS ET_0 in the medium range (5–10 mm) is not as good. In case of high ET_0 (10–15 mm) category, both datasets exhibit degraded performance, but the estimated gridded ET_0 shows a relatively higher probability of detection with a POD of 0.4 and SR of 0.9 than the GLDAS ET_0 .

4. Summary and Conclusions

This paper examines the spatiotemporal distribution of reference evapotranspiration (ET_0) patterns across various meteorological regions of India. The study proposed a gridded ET_0 dataset which is generated through the integration of observed gridded data, model reanalysis products, and satellite data. Furthermore, the study includes a comprehensive statistical comparison with station estimates and other available sources as well, such as the GLDAS model ET_0 . The analysis highlights the importance of monitoring evapotranspiration, especially in rainfed regions and during climate variability, for effective climate risk management and agricultural planning. Different regions of India show varying levels of annual and temporal variability in ET_0 values, with coastal and hilly areas showing lower variability compared to regions like Rajasthan, Gujarat, Madhya Pradesh, Bihar, and Uttar Pradesh. Calibration of

various model based ET_0 is crucial for precise advisories to farmers and planners. The study employs a linear bias correction method and suggests conducting seasonal calibration to minimize errors introduced by input parameters. The analysis demonstrates improvements in accuracy and correlation between estimated gridded ET_0 and station ET_0 values after calibration. However, discrepancies still exist, particularly in coastal and hilly regions, indicating the need for further improvement in those areas. The study also compares the GLDAS model-based ET_0 with station-estimated ET_0 . GLDAS ET_0 tends to overestimate values and requires calibration for practical use. The analysis shows varying levels of agreement and accuracy between GLDAS ET_0 and station ET_0 across different meteorological subdivisions and seasons. Probability of detection (POD) analysis is also performed to assess the performance of estimated gridded ET_0 and GLDAS ET_0 in different ET_0 value categories. The estimated gridded ET_0 demonstrates better performance, particularly in the high ET_0 range, compared to GLDAS ET_0 .

The finding of this study can also contribute to the global model datasets to calibrate the models at the regional level. In developing countries like India, establishing and maintaining a dense network of observatories for reliable and accurate weather data is challenging. However, leveraging satellite data and high-resolution models in the current era allows for capturing spatial variability and identifying vulnerable areas, enabling prompt advisories and solutions. In summary, this study highlights the significance of precise ET_0 estimation for agricultural planning, risk management, and irrigation scheduling, while emphasizing the regional and seasonal variations in ET_0 patterns across India.

Declarations

Funding

This research received no external funding.

Conflicts of interest/Competing interests

The authors declare no conflict of interest and no funders had any role in the design of the study; in the collection, analyses, or interpretation of data; in the writing of the manuscript; or in the decision to publish the results.

Availability of data and material

The data that support the findings of this study are available from the corresponding author upon reasonable request.

Author Contributions

Conceptualizations: Anil Kumar Soni, Jayant Nath Tripathi, K. K. Singh, Kripan Ghosh; Software: Anil Kumar Soni, M. Sateesh; Resources: Kripan Ghosh, Priyanka Singh, K. K. Singh, Jayant Nath Tripathi;

Data curation: Anil Kumar Soni, M. Sateesh, Priyanka Singh; Writing: Anil Kumar Soni, Priyanka Singh, M. Sateesh, Kripan Ghosh; Review and editing: Jayant Nath Tripathi, Kripan Ghosh, K. K. Singh. All authors have read and agreed to the published version of the manuscript.

Acknowledgments

The authors wish to acknowledge the continuous support and data from the project “Gramin Krishi Mausam Sewa” (GKMS) under Indian Meteorological Department (MoES), Government of India to conduct this study. Authors would also like to thank DGM, India Meteorological Department for his encouragement towards the development of satellite and ground observation based potential evapotranspiration product to help the Agromet Advisory services.

References

1. Abdollahnejad, A., Panagiotidis, D., Surový, P., 2018. Estimation and Extrapolation of Tree Parameters Using Spectral Correlation between UAV and Pléiades Data. *Forests* 9, 85. <https://doi.org/10.3390/f9020085>
2. Abeysekara, W.C.S.M., Siriwardana, M., Meng, S., 2023. Economic consequences of climate change impacts on the agricultural sector of South Asia: A case study of Sri Lanka. *Econ Anal Policy* 77, 435–450. <https://doi.org/10.1016/j.eap.2022.12.003>
3. Allen, R.G., Pereira, L.S., Raes, D., Smith, M., 1998a. FAO Irrigation and Drainage Paper No. 56 - Crop Evapotranspiration. <https://www.fao.org/3/X0490E/x0490e00.htm>
4. Allen, R.G., Pereira, L.S., Raes, D., Smith, M., 1998b. FAO Irrigation and Drainage Paper No. 56 - Crop Evapotranspiration.
5. ANNUAL REPORT 2020-21, 2021nn. New Delhi. <https://agricoop.nic.in/Documents/annual-report-2020-21.pdf> Accessed on 1 April 2023
6. Attia, A., Govind, A., Qureshi, A.S., Feike, T., Rizk, M.S., Shabana, M.M.A., Kheir, A.M.S., 2022. Coupling Process-Based Models and Machine Learning Algorithms for Predicting Yield and Evapotranspiration of Maize in Arid Environments. *Water (Basel)* 14, 3647. <https://doi.org/10.3390/w14223647>
7. Baik, J., Choi, M., 2015. Evaluation of geostationary satellite (COMS) based Priestley-Taylor evapotranspiration. *Agric Water Manag* 159, 77–91. <https://doi.org/10.1016/j.agwat.2015.05.017>
8. Bhattacharya, B.K., Padmanabhan, N., Mahammed, S., Ramakrishnan, R., Parihar, J.S., 2013. Assessing solar energy potential using diurnal remote-sensing observations from Kalpana-1 VHRR and validation over the Indian landmass. *Int J Remote Sens* 34, 7069–7090. <https://doi.org/10.1080/01431161.2013.811311>
9. Bhattarai, N., Shaw, S.B., Quackenbush, L.J., Im, J., Niraula, R., 2016. Evaluating five remote sensing based single-source surface energy balance models for estimating daily evapotranspiration in a humid subtropical climate. *International Journal of Applied Earth Observation and Geoinformation* 49, 75–86. <https://doi.org/10.1016/j.jag.2016.01.010>

10. Bois, B., Pieri, P., Van Leeuwen, C., Wald, L., Huard, F., Gaudillere, J.P., Saur, E., 2008. Using remotely sensed solar radiation data for reference evapotranspiration estimation at a daily time step. *Agric For Meteorol* 148, 619–630. <https://doi.org/10.1016/j.agrformet.2007.11.005>
11. Buehner, M., Morneau, J., Charette, C., 2013. Four-dimensional ensemble-variational data assimilation for global deterministic weather prediction. *Nonlinear Process Geophys* 20, 669–682. <https://doi.org/10.5194/npg-20-669-2013>
12. Cahn, M., Johnson, L., 2017. New Approaches to Irrigation Scheduling of Vegetables. *Horticulturae* 3, 28. <https://doi.org/10.3390/horticulturae3020028>
13. Chen, N., Li, X., Shi, H., Zhang, Y., Hu, Q., Sun, Y., 2023. Modeling effects of biodegradable film mulching on evapotranspiration and crop yields in Inner Mongolia. *Agric Water Manag* 275, 107996. <https://doi.org/10.1016/j.agwat.2022.107996>
14. Choudhury, B.J., 1997. Global pattern of potential evaporation calculated from the Penman-Monteith equation using satellite and assimilated data. *Remote Sens Environ* 61, 64–81. [https://doi.org/10.1016/S0034-4257\(96\)00241-6](https://doi.org/10.1016/S0034-4257(96)00241-6)
15. Cruz-Blanco, M., Lorite, I.J., Santos, C., 2014. An innovative remote sensing based reference evapotranspiration method to support irrigation water management under semi-arid conditions. *Agric Water Manag* 131, 135–145. <https://doi.org/10.1016/j.agwat.2013.09.017>
16. George H. Hargreaves, Zohrab A. Samani, 1985. Reference Crop Evapotranspiration from Temperature. *Appl Eng Agric* 1, 96–99. <https://doi.org/10.13031/2013.26773>
17. Heck, K., Coltman, E., Schneider, J., Helwig, R., 2020. Influence of Radiation on Evaporation Rates: A Numerical Analysis. *Water Resour Res* 56. <https://doi.org/10.1029/2020WR027332>
18. Huerta, A., Bonnesoeur, V., Cuadros-Adriazola, J., Gutierrez, L., Ochoa-Tocachi, B.F., Román-Dañobeytia, F., Lavado-Casimiro, W., 2022. PISCOeo_pm, a reference evapotranspiration gridded database based on FAO Penman-Monteith in Peru. *Sci Data* 9, 328. <https://doi.org/10.1038/s41597-022-01373-8>
19. Jarvis, A., Reuter, H.I., Nelson, A., Guevara, E., others, 2008. Hole-filled SRTM for the globe Version 4. available from the CGIAR-CSI SRTM 90m Database (<http://srtm.csi.cgiar.org>) 15, 5.
20. Jha, P., Chinngaihlian, S., Upreti, P., Handa, A., 2023. A machine learning approach to assess implications of Climate Risk Factors on Agriculture: The Indian case. *Clim Risk Manag* 100523. <https://doi.org/10.1016/j.crm.2023.100523>
21. Kamath, H.G., Srinivasan, J., 2020. Validation of global irradiance derived from INSAT-3D over India. *Solar Energy* 202, 45–54. <https://doi.org/10.1016/j.solener.2020.03.084>
22. Kite, G., 2000. Using a basin-scale hydrological model to estimate crop transpiration and soil evaporation. *J Hydrol (Amst)* 229, 59–69. [https://doi.org/10.1016/S0022-1694\(99\)00199-7](https://doi.org/10.1016/S0022-1694(99)00199-7)
23. Kumar, A., Sridevi, C., Durai, V.R., Singh, K.K., Mukhopadhyay, P., Chattopadhyay, N., 2019. MOS guidance using a neural network for the rainfall forecast over India. *Journal of Earth System Science* 128, 1–12. <https://doi.org/10.1007/s12040-019-1149-y>

24. Lee, K.-H., 2010. Relative Comparison of the Local Recalibration of the Temperature-Based Evapotranspiration Equation for the Korea Peninsula. *Journal of Irrigation and Drainage Engineering* 136, 585–594. [https://doi.org/10.1061/\(ASCE\)IR.1943-4774.0000221](https://doi.org/10.1061/(ASCE)IR.1943-4774.0000221)
25. Lee, S., Qi, J., McCarty, G.W., Anderson, M., Yang, Y., Zhang, X., Moglen, G.E., Kwak, D., Kim, H., Lakshmi, V., Kim, S., 2022. Combined use of crop yield statistics and remotely sensed products for enhanced simulations of evapotranspiration within an agricultural watershed. *Agric Water Manag* 264, 107503. <https://doi.org/10.1016/j.agwat.2022.107503>
26. Lorite, I.J., García-Vila, M., Carmona, M.-A., Santos, C., Soriano, M.-A., 2012. Assessment of the Irrigation Advisory Services' Recommendations and Farmers' Irrigation Management: A Case Study in Southern Spain. *Water Resources Management* 26, 2397–2419. <https://doi.org/10.1007/s11269-012-0023-3>
27. Malek, E., 1994. Calibration of the Penman wind function using the Bowen ratio energy balance method. *J Hydrol (Amst)* 163, 289–298. [https://doi.org/10.1016/0022-1694\(94\)90145-7](https://doi.org/10.1016/0022-1694(94)90145-7)
28. Monteith, J.L., 1981. Evaporation and surface temperature. *Quarterly Journal of the Royal Meteorological Society* 107, 1–27. <https://doi.org/10.1002/qj.49710745102>
29. Nash, J.E., Sutcliffe, J.V., 1970. River flow forecasting through conceptual models part I – A discussion of principles. *J Hydrol (Amst)* 10, 282–290. [https://doi.org/10.1016/0022-1694\(70\)90255-6](https://doi.org/10.1016/0022-1694(70)90255-6)
30. Ondrasek, G., 2014. Water Scarcity and Water Stress in Agriculture, in: *Physiological Mechanisms and Adaptation Strategies in Plants Under Changing Environment*. Springer New York, New York, NY, pp. 75–96. https://doi.org/10.1007/978-1-4614-8591-9_4
31. PENMAN, H.L., 1948. Natural evaporation from open water, bare soil and grass. *Proc R Soc Lond A Math Phys Sci* 193, 120–145. <https://doi.org/10.1098/rspa.1948.0037>
32. Pereira, L.S., Perrier, A., Allen, R.G., Alves, I., 1999. Evapotranspiration: Concepts and Future Trends. *Journal of Irrigation and Drainage Engineering* 125, 45–51. [https://doi.org/10.1061/\(ASCE\)0733-9437\(1999\)125:2\(45\)](https://doi.org/10.1061/(ASCE)0733-9437(1999)125:2(45))
33. PRIESTLEY, C.H.B., TAYLOR, R.J., 1972. On the Assessment of Surface Heat Flux and Evaporation Using Large-Scale Parameters. *Mon Weather Rev* 100, 81–92. [https://doi.org/10.1175/1520-0493\(1972\)100<0081:otaosh>2.3.co;2](https://doi.org/10.1175/1520-0493(1972)100<0081:otaosh>2.3.co;2)
34. Rajeevan, M.N., Nayak, S., 2017 Springer Geology Observed Climate Variability and Change over the Indian Region. <https://doi.org/10.1007/978-981-10-2531-0>
35. Rao, B.B., Sandeep, V.M., Rao, V.U.M., Venkateswarlu, B., 2012. Potential Evapotranspiration estimation for Indian conditions: Improving accuracy through calibration coefficients, Tech. Bull No 1/2012. ed. The Director, Central Research Institute for Dryland Agriculture, Hyderabad.
<http://www.nicra-icar.in/nicrarevised/images/Books/Potential%20Evapotranspiration%20estimation.pdf> Accessed on 25 Aug 2022

36. Rodell, M., Houser, P.R., Jambor, U., Gottschalck, J., Mitchell, K., Meng, C.J., Arsenault, K., Cosgrove, B., Radakovich, J., Bosilovich, M., Entin, J.K., Walker, J.P., Lohmann, D., Toll, D., 2004. The Global Land Data Assimilation System. *Bull Am Meteorol Soc* 85, 381–394. <https://doi.org/10.1175/BAMS-85-3-381>
37. Roebber, P.J., 2009. Visualizing Multiple Measures of Forecast Quality. *Weather Forecast* 24, 601–608. <https://doi.org/10.1175/2008WAF2222159.1>
38. S. Ha, W., R. Diak, G., F. Krajewski, W., 2020. Estimating Near Real-Time Hourly Evapotranspiration Using Numerical Weather Prediction Model Output and GOES Remote Sensing Data in Iowa. *Remote Sens (Basel)* 12, 2337. <https://doi.org/10.3390/rs12142337>
39. Sela, J., 2010. The derivation of the sigma pressure hybrid coordinate semi-Lagrangian model equations for the GFS. *NCEP Office Note* 462, pp31.
https://repository.library.noaa.gov/view/noaa/6971/noaa_6971_DS1.pdf
40. Singer, M.B., Asfaw, D.T., Rosolem, R., Cuthbert, M.O., Miralles, D.G., MacLeod, D., Quichimbo, E.A., Michaelides, K., 2021. Hourly potential evapotranspiration at 0.1° resolution for the global land surface from 1981-present. *Sci Data* 8, 224. <https://doi.org/10.1038/s41597-021-01003-9>
41. Soni, A.K., Tripathi, J.N., Tewari, M., Sateesh, M., Singh, T., 2023a. Future Projection of Drought Risk over Indian Meteorological Subdivisions Using Bias-Corrected CMIP6 Scenarios. *Atmosphere (Basel)* 14, 725. <https://doi.org/10.3390/atmos14040725>
42. Soni, A.K., Tripathi, J.N., Tewari, M., Sateesh, M., Singh, T., 2023b. Future Projection of Drought Risk over Indian Meteorological Subdivisions Using Bias-Corrected CMIP6 Scenarios. *Atmosphere (Basel)* 14, 725. <https://doi.org/10.3390/atmos14040725>
43. Sridevi, C., Singh, K.K., Suneetha, P., Durai, V.R., Kumar, A., 2020. Rainfall forecasting skill of GFS model at T1534 and T574 resolution over India during the monsoon season. *Meteorology and Atmospheric Physics* 132, 35–52. <https://doi.org/10.1007/s00703-019-00672-x>
44. Srivastava, A.K., Rajeevan, M., Kshirsagar, S.R., 2009. Development of a high resolution daily gridded temperature data set (1969-2005) for the Indian region. *Atmospheric Science Letters* n/a-n/a.
<https://doi.org/10.1002/asl.232>
45. Subedi, A., Chávez, J.L., 2015. Crop Evapotranspiration (ET) Estimation Models: A Review and Discussion of the Applicability and Limitations of ET Methods. *Journal of Agricultural Science* 7.
<https://doi.org/10.5539/jas.v7n6p50>
46. Tabari, H., Grismer, M.E., Trajkovic, S., 2013. Comparative analysis of 31 reference evapotranspiration methods under humid conditions. *Irrig Sci* 31, 107–117. <https://doi.org/10.1007/s00271-011-0295-z>
47. Tanahashi, S., Kawamura, H., Matsuura, T., Takahashi, T., Yusa, H., 2001. A system to distribute satellite incident solar radiation in real-time. *Remote Sens Environ* 75, 412–422.
[https://doi.org/10.1016/S0034-4257\(00\)00183-8](https://doi.org/10.1016/S0034-4257(00)00183-8)
48. Tarpley, J.D., 1979. Estimating Incident Solar Radiation at the Surface from Geostationary Satellite Data. *J Appl Meteorol Climatol* 18, 1172–1181. [https://doi.org/10.1175/1520-0450\(1979\)018<1172:EISRAT>2.0.CO;2](https://doi.org/10.1175/1520-0450(1979)018<1172:EISRAT>2.0.CO;2)

49. Thornthwaite, C.W. (1948) An Approach toward a Rational Classification of Climate. *Geographical Review*, 38, 55-94. <http://dx.doi.org/10.2307/210739>
50. Vishwakarma, D.K., Pandey, K., Kaur, A., Kushwaha, N.L., Kumar, R., Ali, R., Elbeltagi, A., Kuriqi, A., 2022. Methods to estimate evapotranspiration in humid and subtropical climate conditions. *Agric Water Manag* 261, 107378. <https://doi.org/10.1016/j.agwat.2021.107378>
51. Vyas, S.S., Nigam, R., Bhattacharya, B.K., Kumar, P., 2016. Development of real-time reference evapotranspiration at the regional scale using satellite-based observations. *Int J Remote Sens* 37, 6108–6126. <https://doi.org/10.1080/01431161.2016.1253895>
52. Wu, H., Yue, Q., Guo, P., Xu, X., Huang, X., 2022. Improving the AquaCrop model to achieve direct simulation of evapotranspiration under nitrogen stress and joint simulation-optimization of irrigation and fertilizer schedules. *Agric Water Manag* 266, 107599. <https://doi.org/10.1016/j.agwat.2022.107599>
53. Zhang, K., Kimball, J.S., Running, S.W., 2016. A review of remote sensing based actual evapotranspiration estimation. *WIREs Water* 3, 834–853. <https://doi.org/10.1002/wat2.1168>
54. Zhang, Q., Akhtar, R., Saif, A.N.M., Akhter, H., Hossan, D., Alam, S.M.A., Bari, Md.F., 2023. The symmetric and asymmetric effects of climate change on rice productivity in Malaysia. *Heliyon* 9, e16118. <https://doi.org/10.1016/j.heliyon.2023.e16118>
55. Zhang, Y., Shen, Y., Sun, H., Gates, J.B., 2011. Evapotranspiration and its partitioning in an irrigated winter wheat field: A combined isotopic and micrometeorologic approach. *J Hydrol (Amst)* 408, 203–211. <https://doi.org/10.1016/j.jhydrol.2011.07.036>
56. Zhang, Y.Q., Chiew, F.H.S., Zhang, L., Leuning, R., Cleugh, H.A., 2008. Estimating catchment evaporation and runoff using MODIS leaf area index and the Penman-Monteith equation. *Water Resour Res* 44, 1–15. <https://doi.org/10.1029/2007WR006563>
57. Zizinga, A., Mwanjalolo, J.-G.M., Tietjen, B., Bedadi, B., Pathak, H., Gabiri, G., Beesigamukama, D., 2022. Climate change and maize productivity in Uganda: Simulating the impacts and alleviation with climate smart agriculture practices. *Agric Syst* 199, 103407. <https://doi.org/10.1016/j.agsy.2022.103407>

Figures

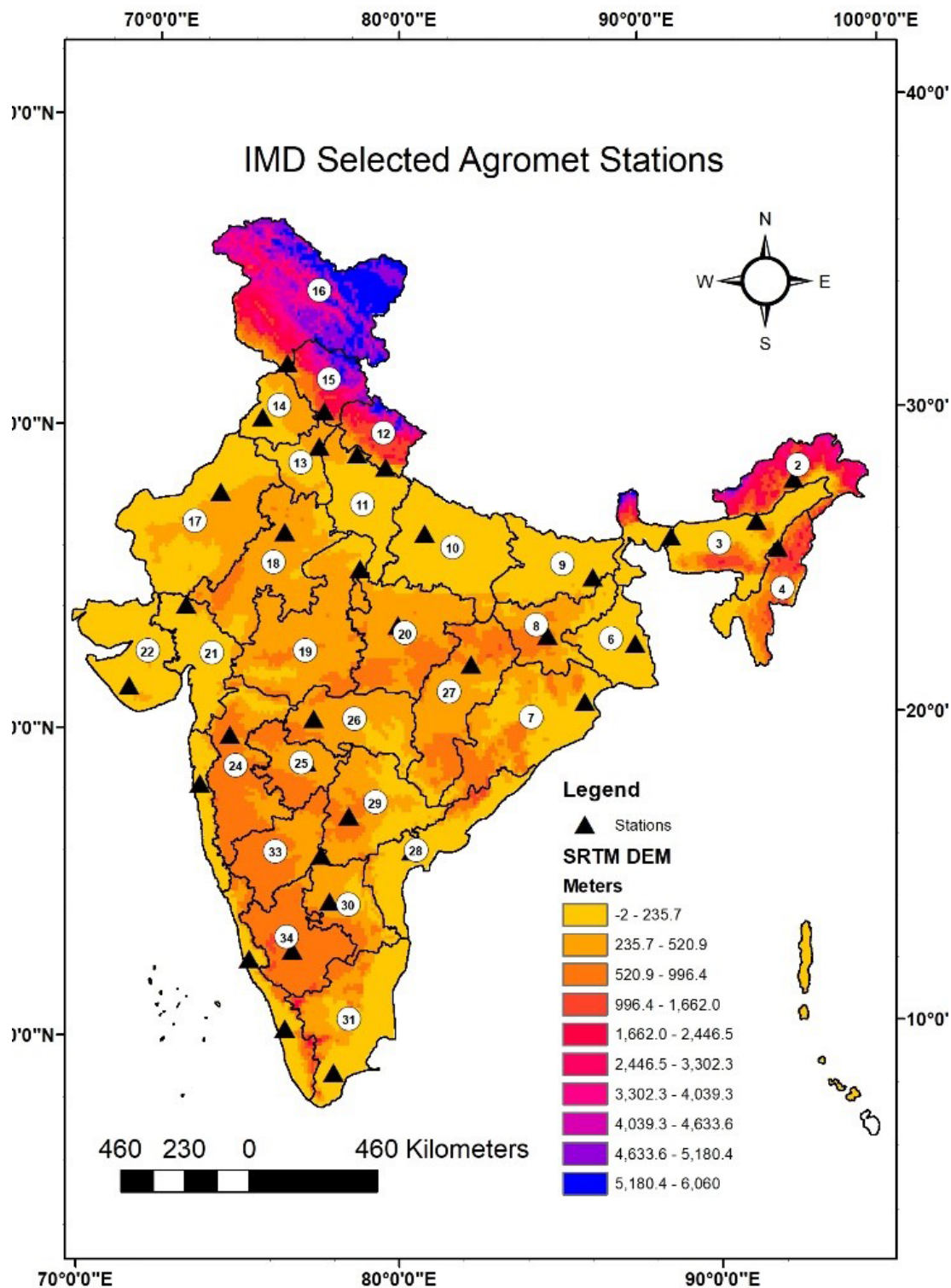


Figure 1

SRTM DEM and spatial distribution of IMD Agromet stations in meteorological subdivisions of India as follows (1. Andaman & Nicobar, 2. Arunachal Pradesh, 3. Assam and Meghalaya, 4. Nagaland-Manipur-Mizoram-Tripura (NMMT), 5. Sub Himalayan West Bengal (SHWB), 6. Gangetic West Bengal, 7. Odisha, 8. Jharkhand, 9. Bihar, 10. East Uttar Pradesh, 11. West Uttar Pradesh, 12. Uttarakhand, 13. Haryana, 14. Punjab, 15. Himachal Pradesh, 16. Jammu & Kashmir, 17. West Rajasthan, 18. East Rajasthan, 19. West

Madhya Pradesh, 20. East Madhya Pradesh, 21. Gujarat Region, 22. Sourashtra, 23. Konkan & Goa, 24. Madhya Maharashtra, 25. Marathwada, 26. Vidarbha, 27. Chhattisgarh, 28. Coastal Andhra Pradesh, 29. Telangana, 30. Rayalaseema, 31. Tamilnadu, 32. Coastal Karnataka, 33. North Interior Karnataka, 34. South Interior Karnataka, 35. Kerala, 36. Lakshadweep).

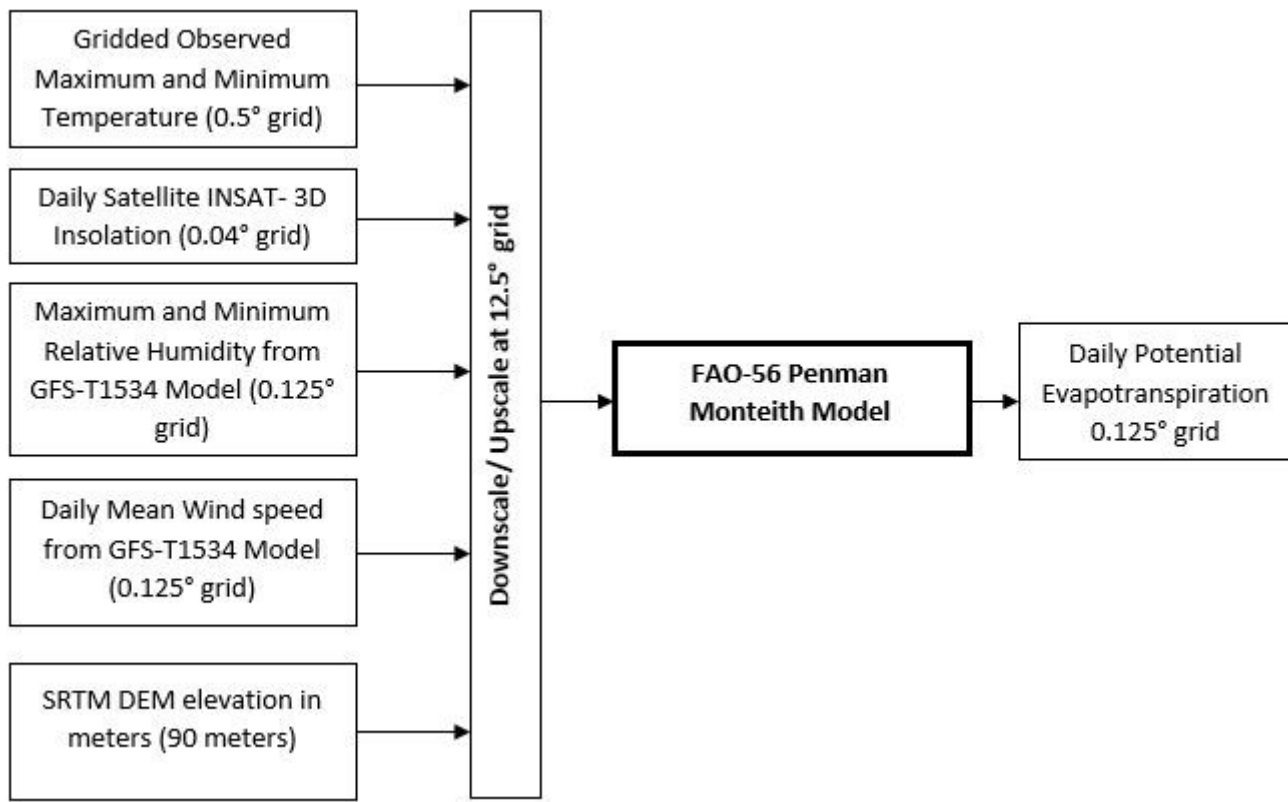


Figure 2

Flow chart to estimate daily ET₀ using FAO-56 Penman Monteith empirical framework

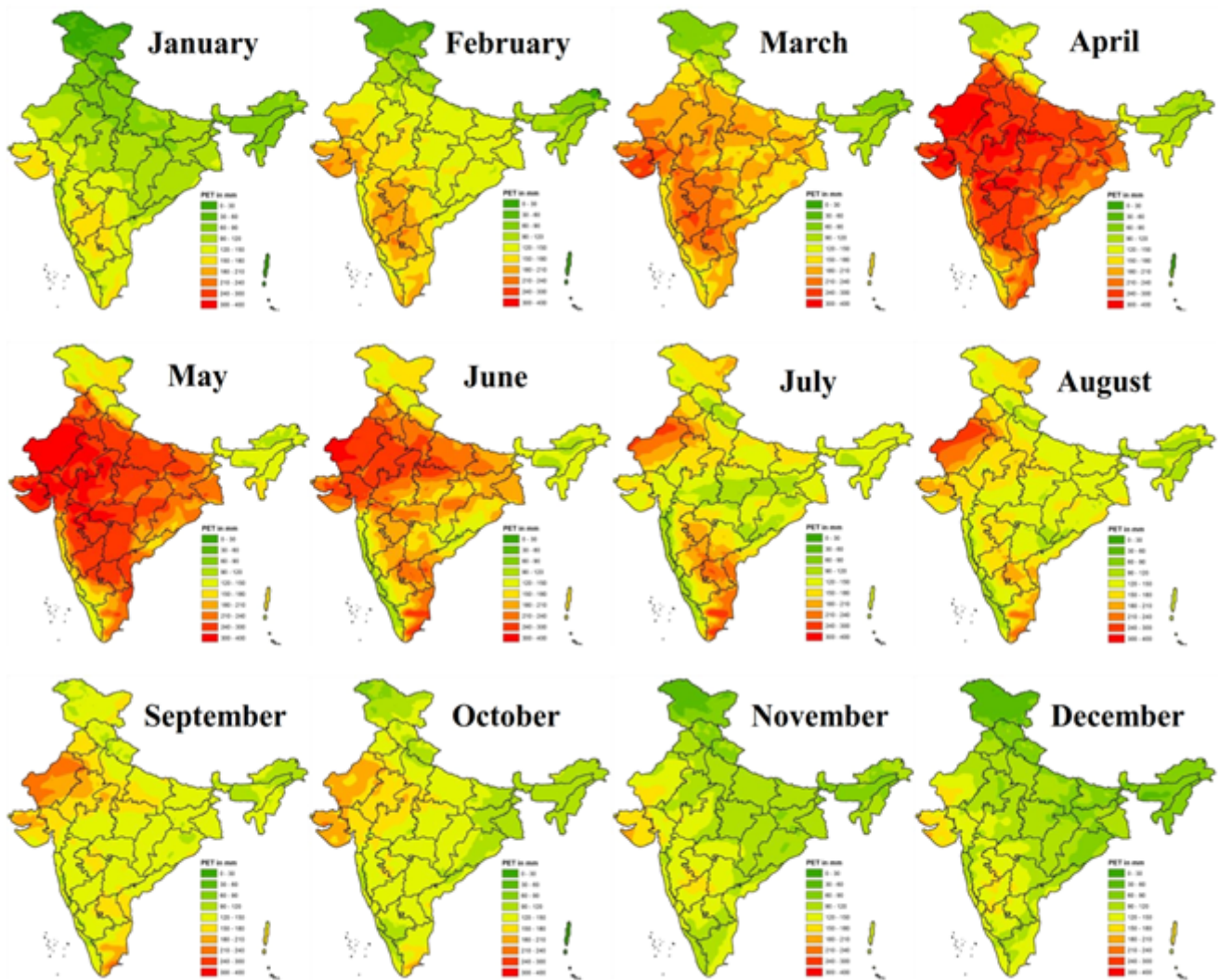


Figure 3

Spatiotemporal distribution of monthly ET_0 over Indian region.

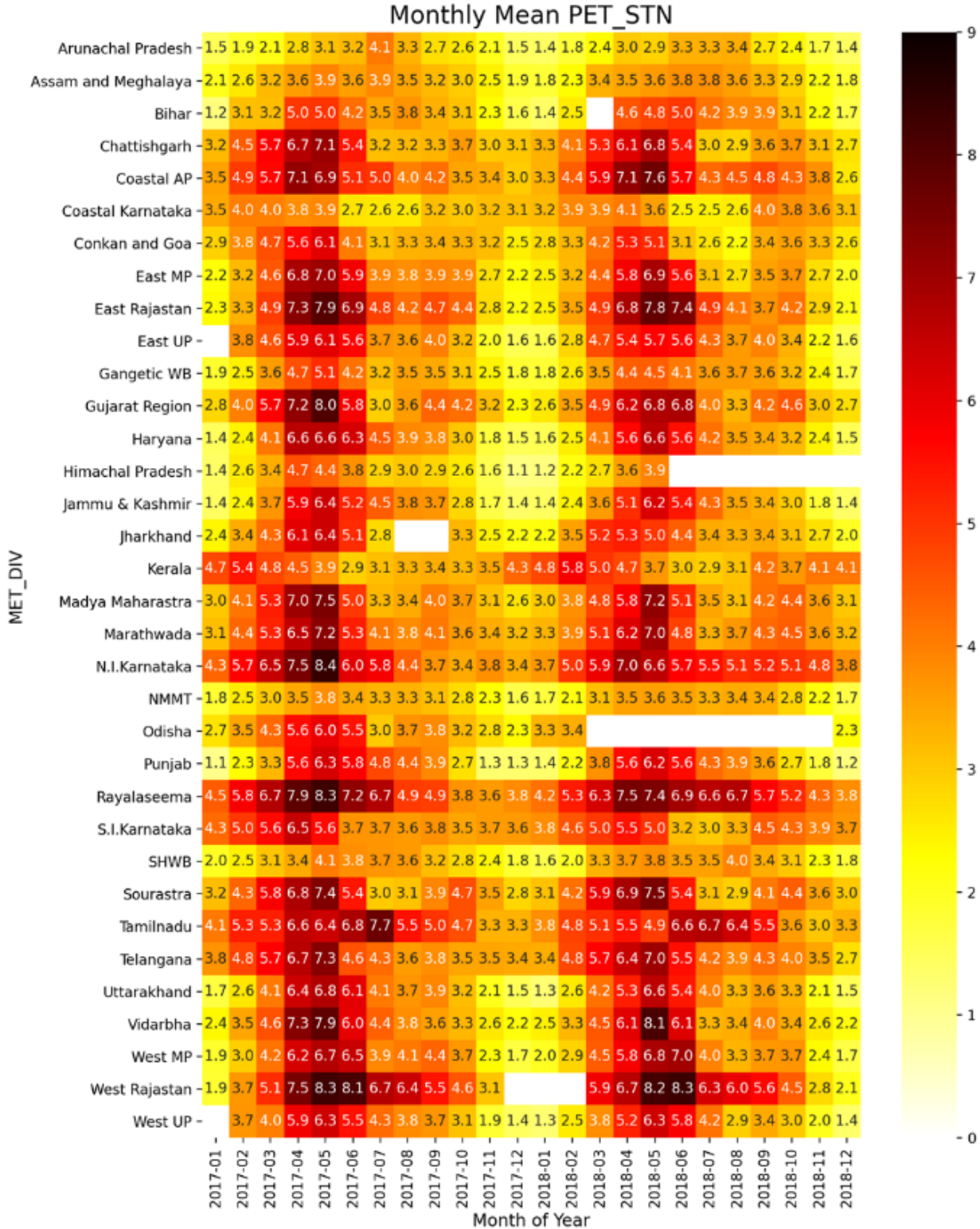


Figure 4

Sub-division wise monthly temporal variation of ET_0

Time Series of Plot

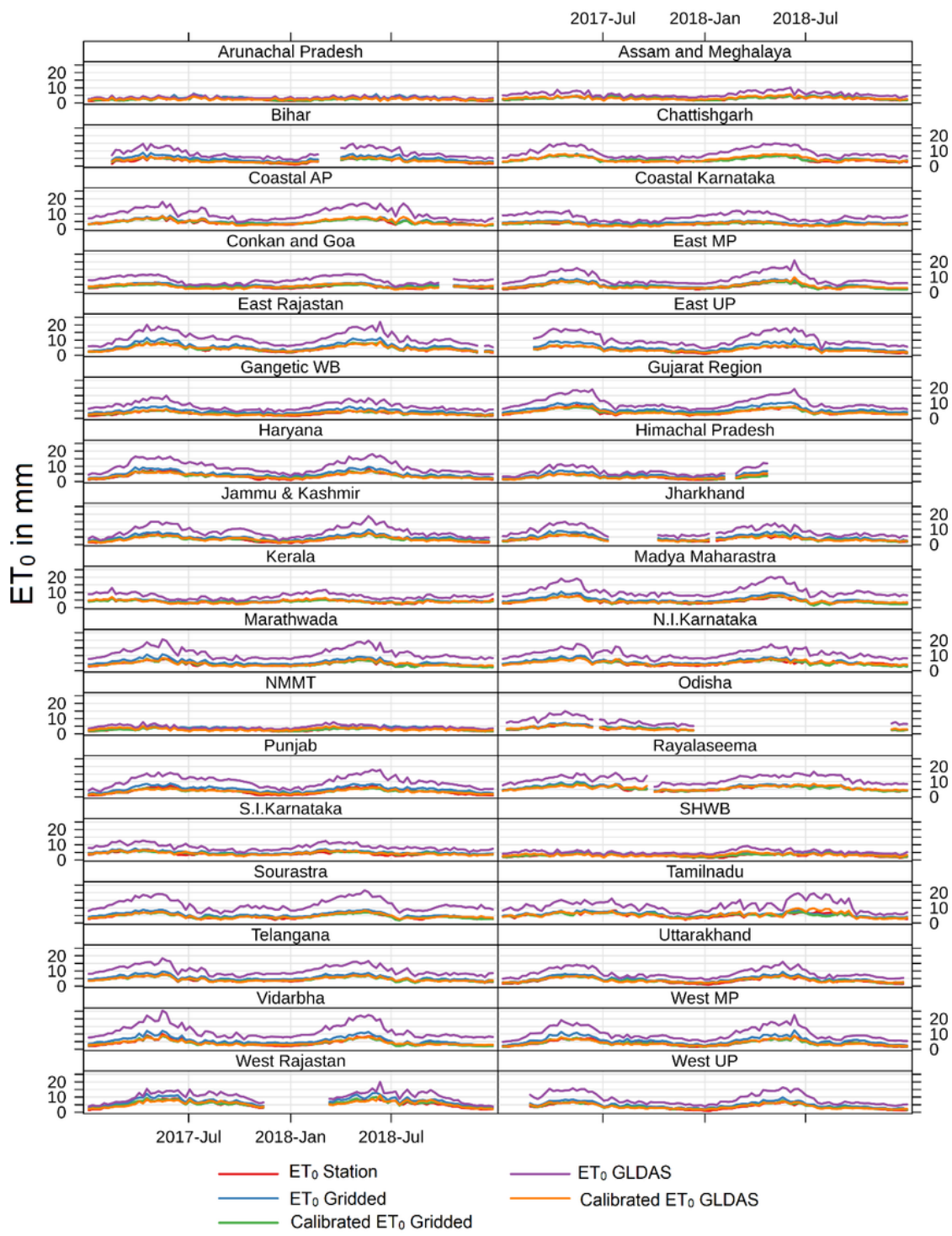


Figure 5

Daily temporal timeseries plot of Estimated gridded ET_0 and GLDAS model ET_0 with station estimated ET_0 for year 2017 and 2018.

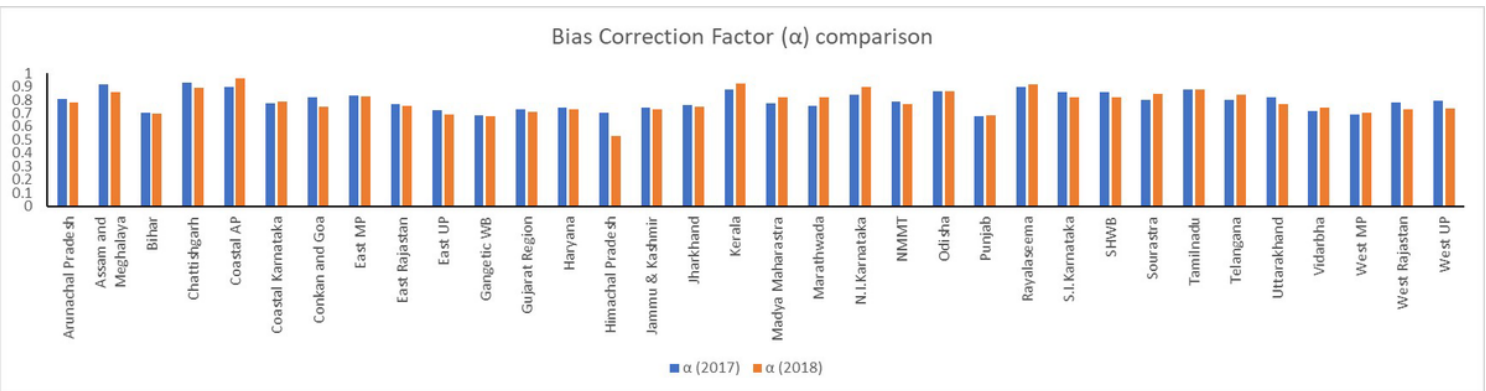


Figure 6

Bias correction factor (α) comparison for year 2017 and 2018

MAPE Comparison of Non calibrated and calibrated gridded ET_0

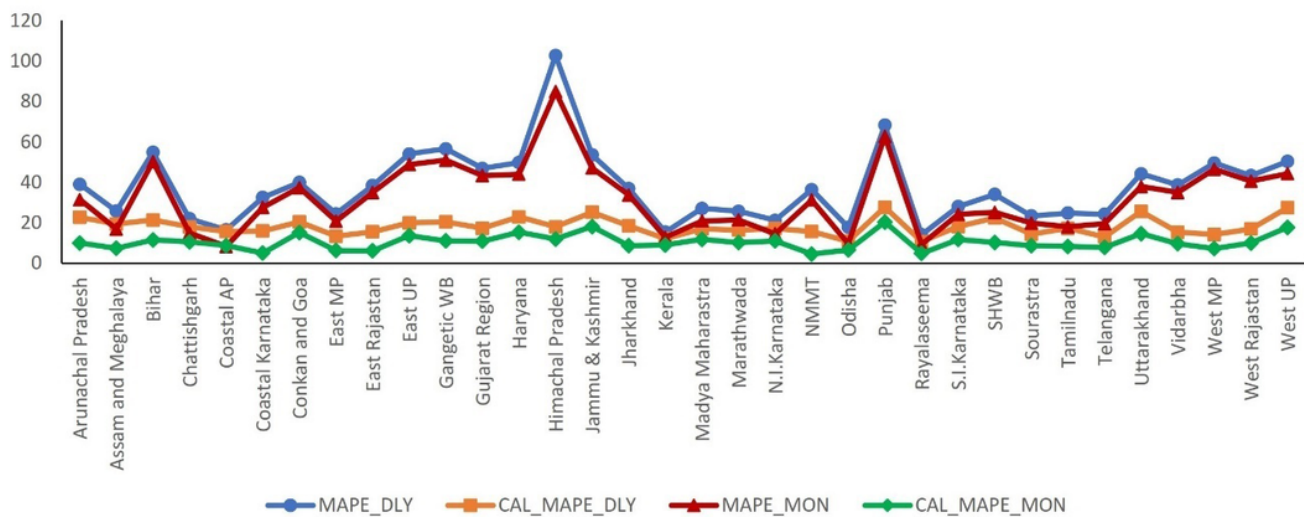


Figure 7

MAPE comparison of Non calibrated and calibrated gridded ET_0 .

NSE Comparison of Non calibrated and calibrated gridded ET_0

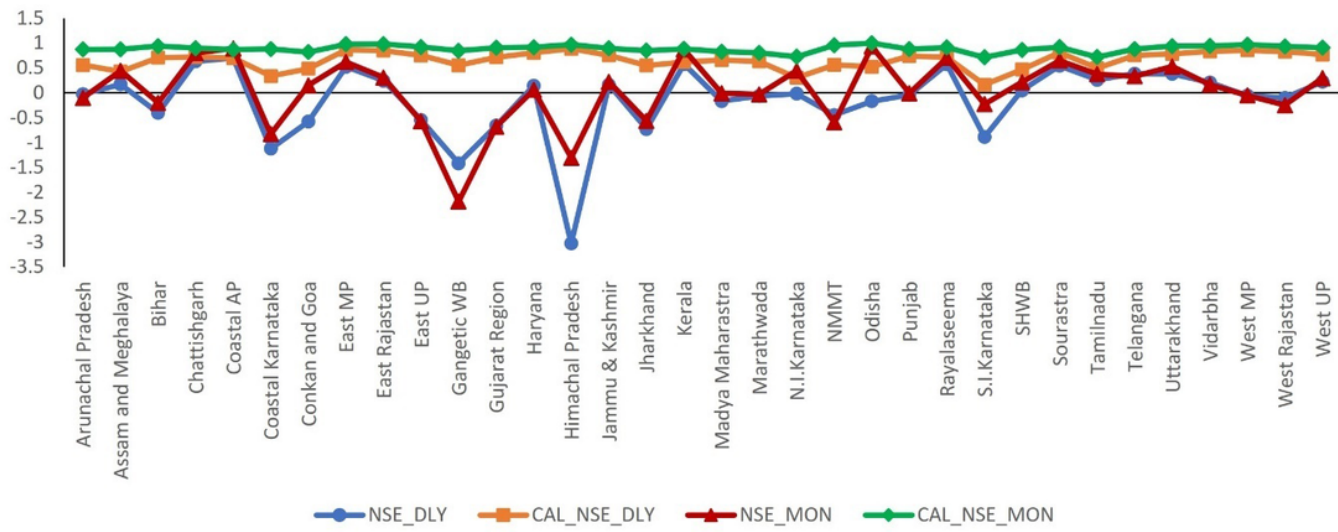


Figure 8

NSE comparison of Non calibrated and calibrated gridded ET_0 .

Coefficient of correlation (R^2) - Station ET_0 and gridded ET_0

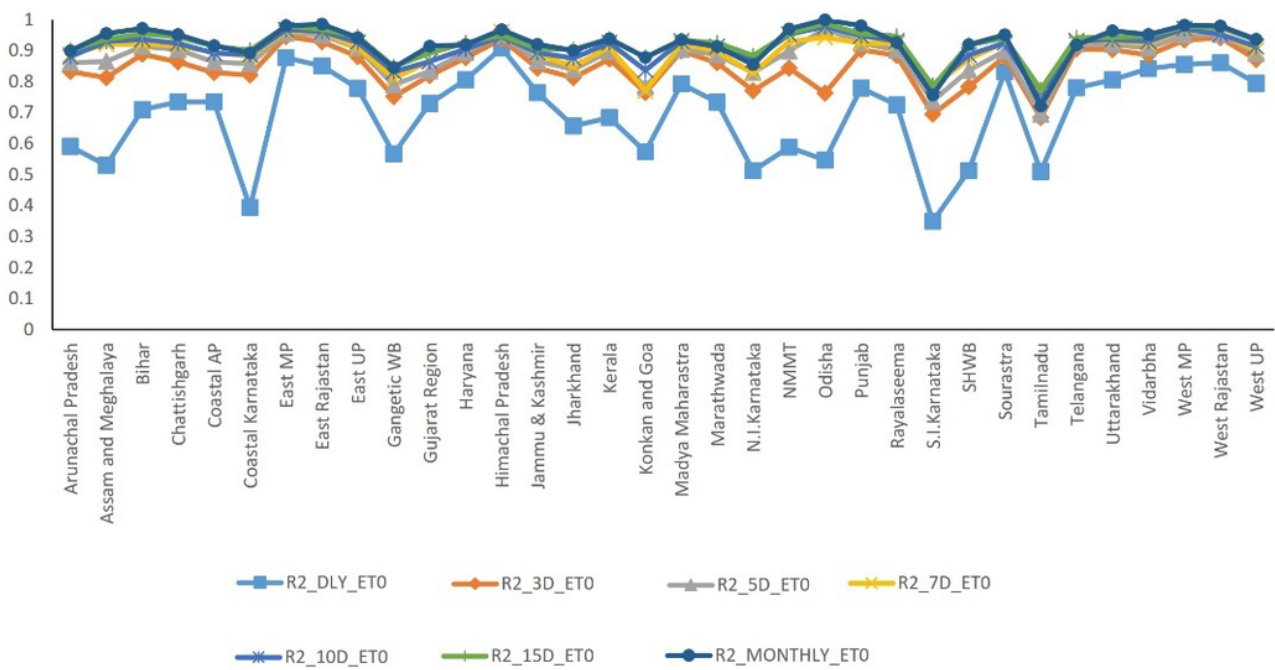


Figure 9

R^2 comparison between estimated station and gridded ET_0 at various temporal scale.

Nash-Sutcliffe Efficiency (NSE) - Station ET_0 and gridded ET_0

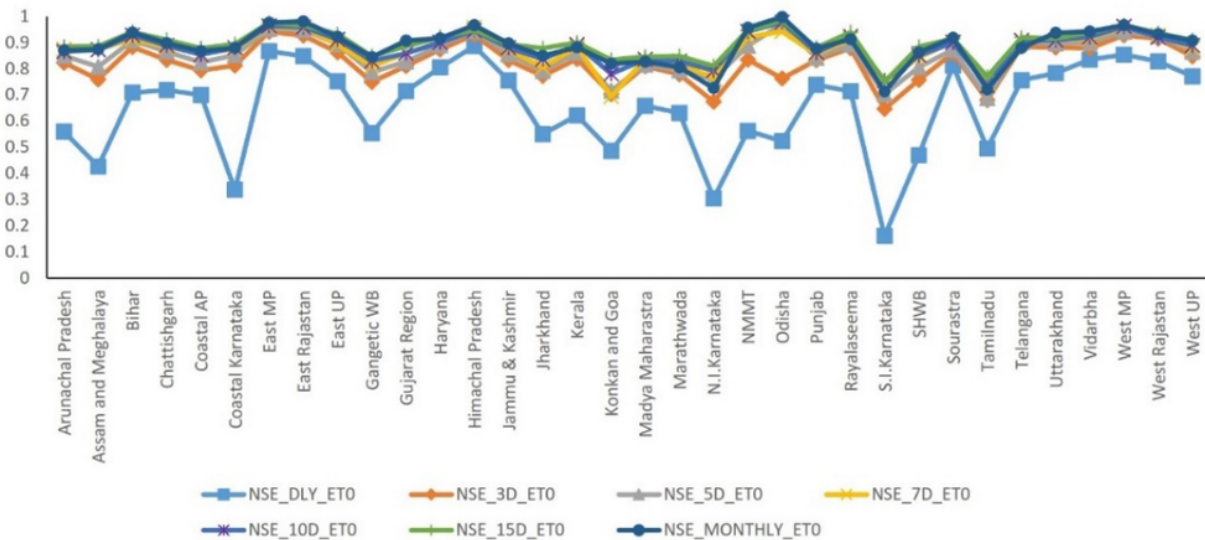


Figure 10

NSE comparison between estimated station and ET_0 gridded at various temporal scale.

Maximum Absolute Percentage Error (MAPE) - Station ET_0 and gridded ET_0

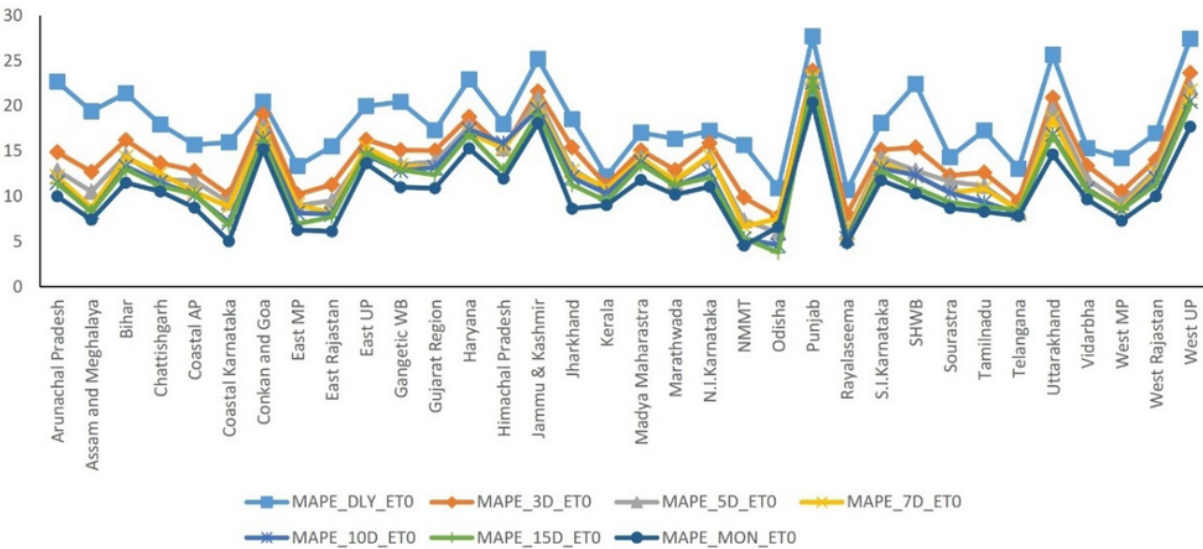


Figure 11

MAPE comparison between estimated station and gridded ET_0 at various temporal scale.

NSE Comparison of Non calibrated and calibrated GLDAS ET_0

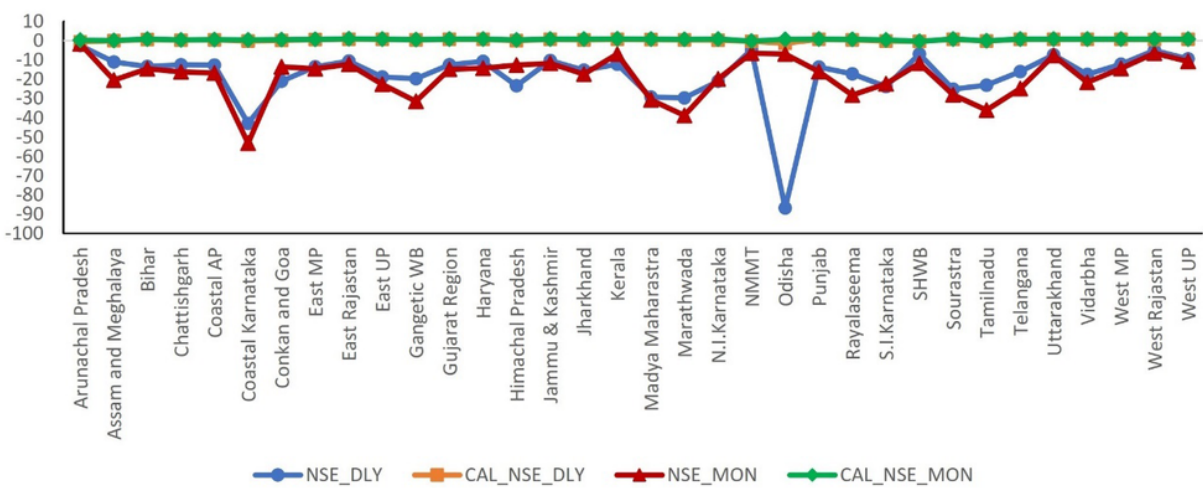


Figure 12

NSE comparison of Non calibrated and calibrated GLDAS ET_0 .

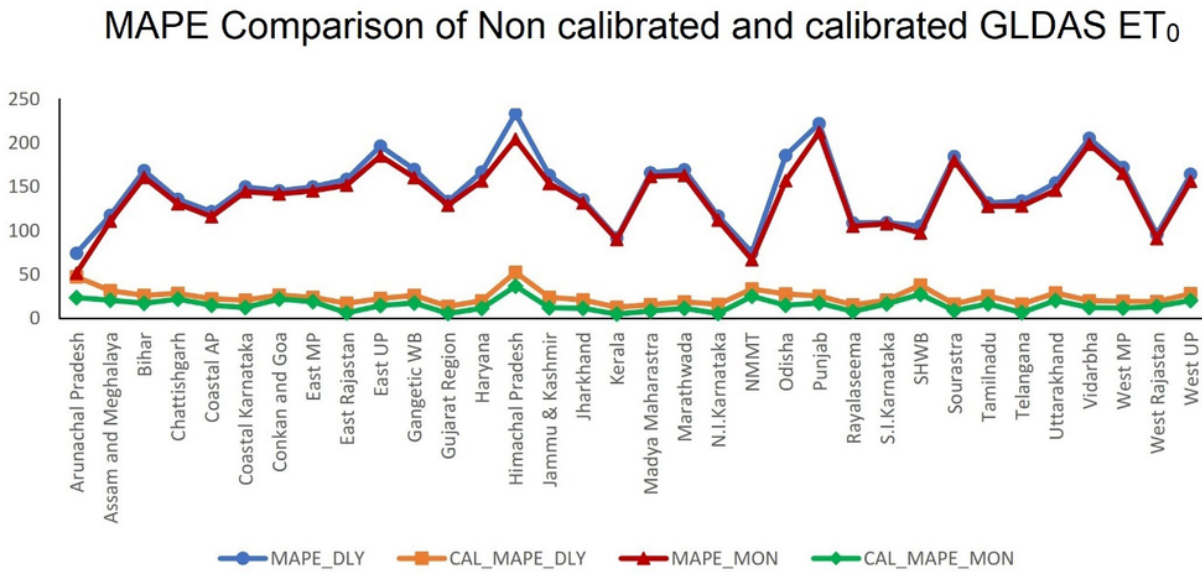


Figure 13

MAPE comparison of Non calibrated and calibrated GLDAS ET_0 .

Coefficient of correlation (R^2) - Station ET_0 and GLDAS ET_0

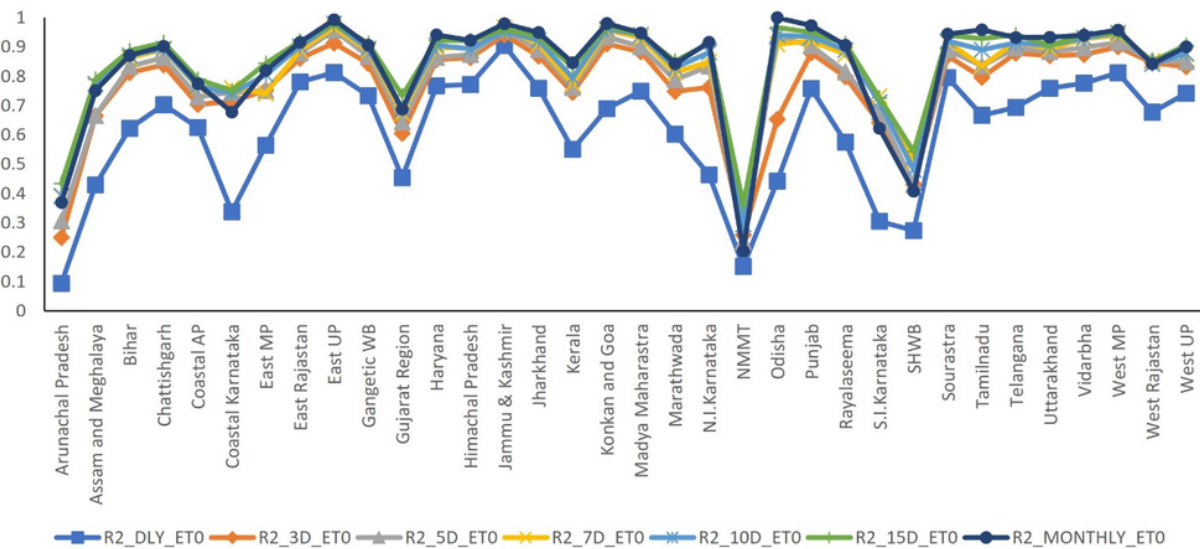


Figure 14

R^2 comparison between estimated station and GLDAS ET_0 at various temporal scale.

Nash-Sutcliffe efficiency (NSE) - Station ET_0 and GLDAS ET_0

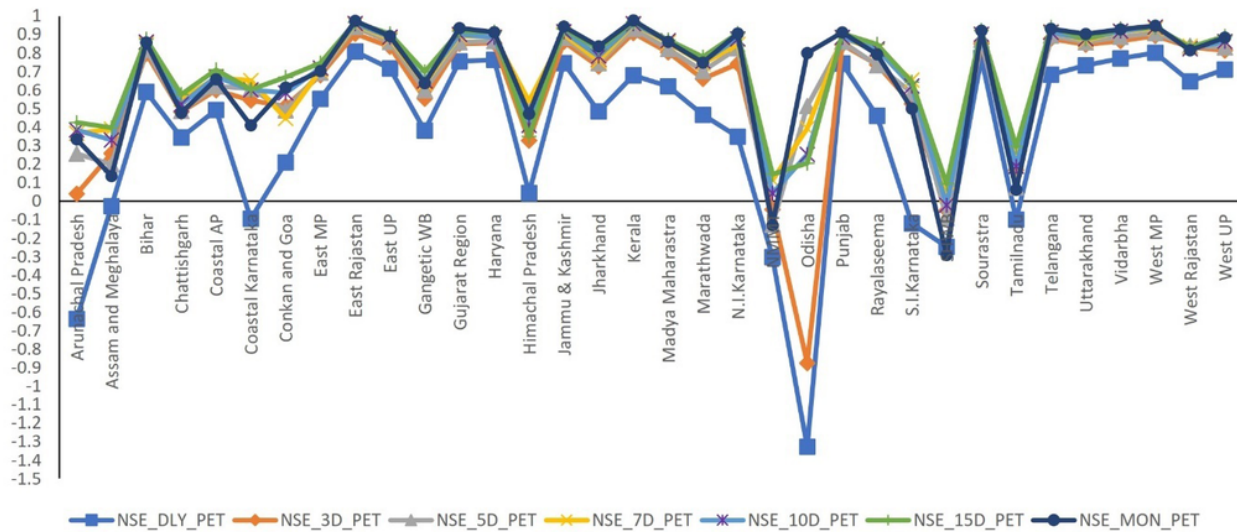


Figure 15

NSE comparison between estimated station and GLDAS ET_0 at various temporal scale.

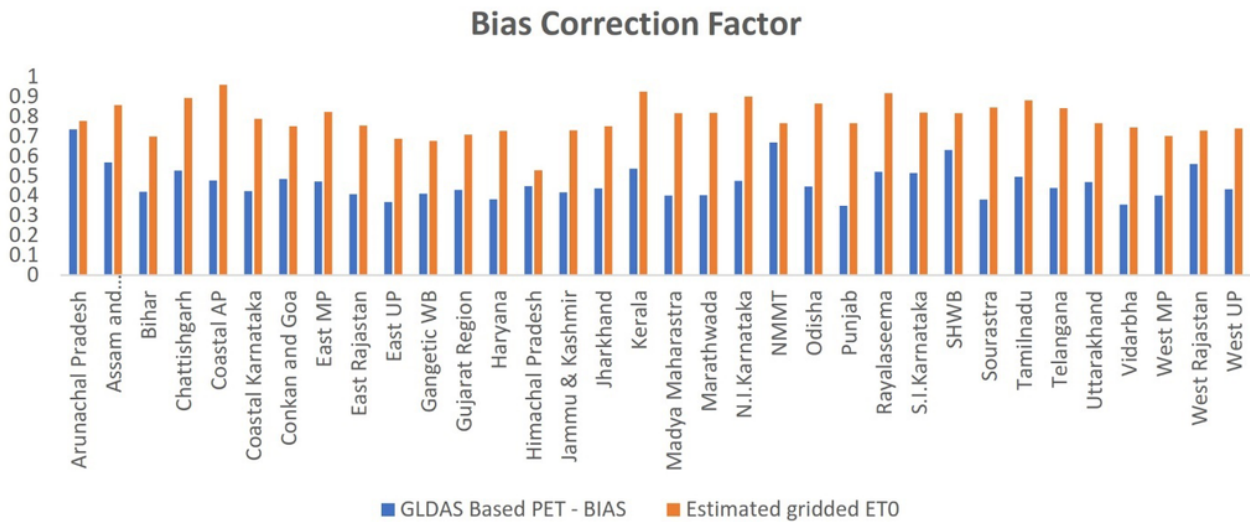


Figure 16

Bias correction factor comparison between GLDAS ET_0 and estimated gridded ET_0 .

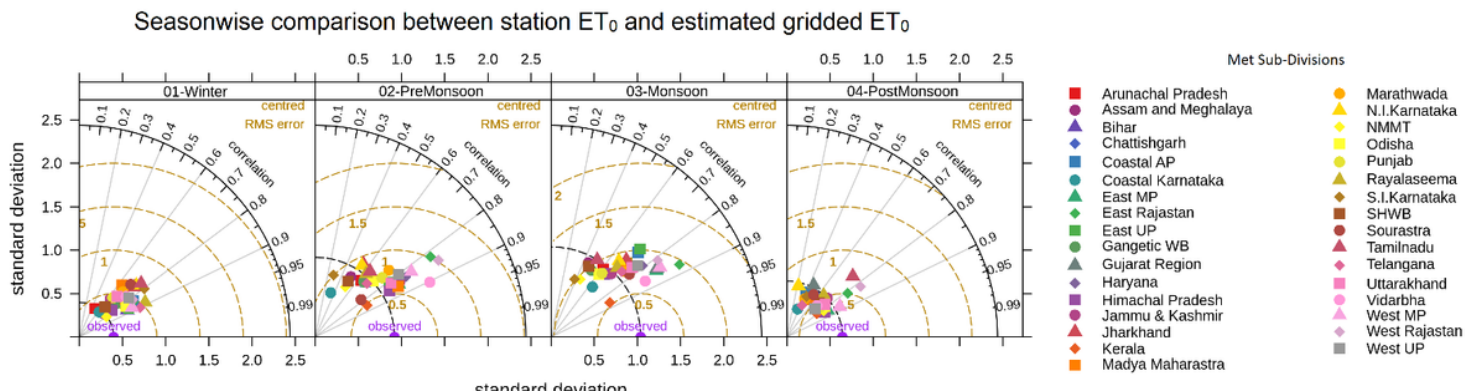


Figure 17

Season wise comparison between Station ET_0 and estimated gridded ET_0 .

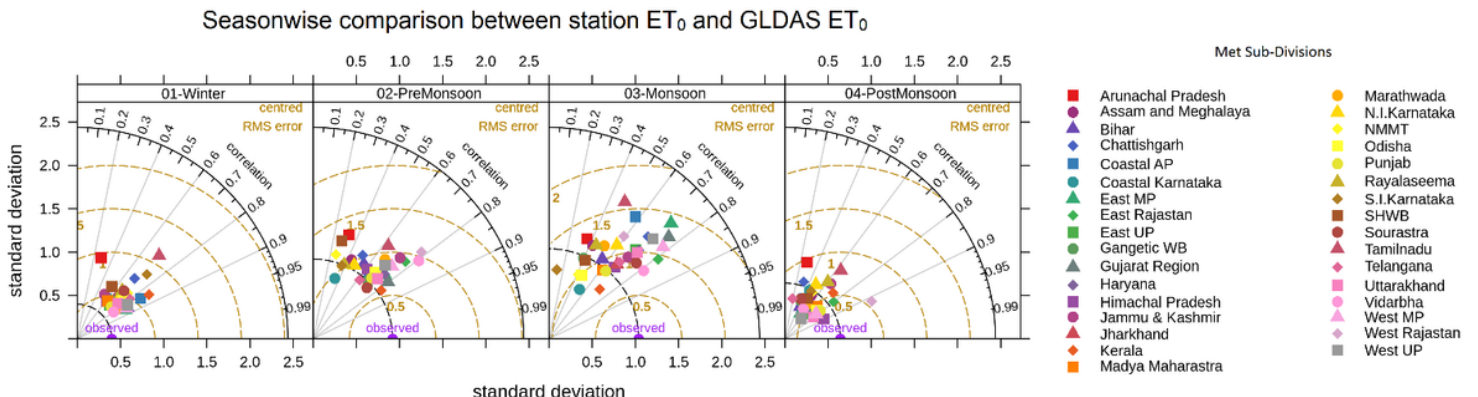


Figure 18

Season wise comparison between Station ET_0 and GLDAS ET_0 .

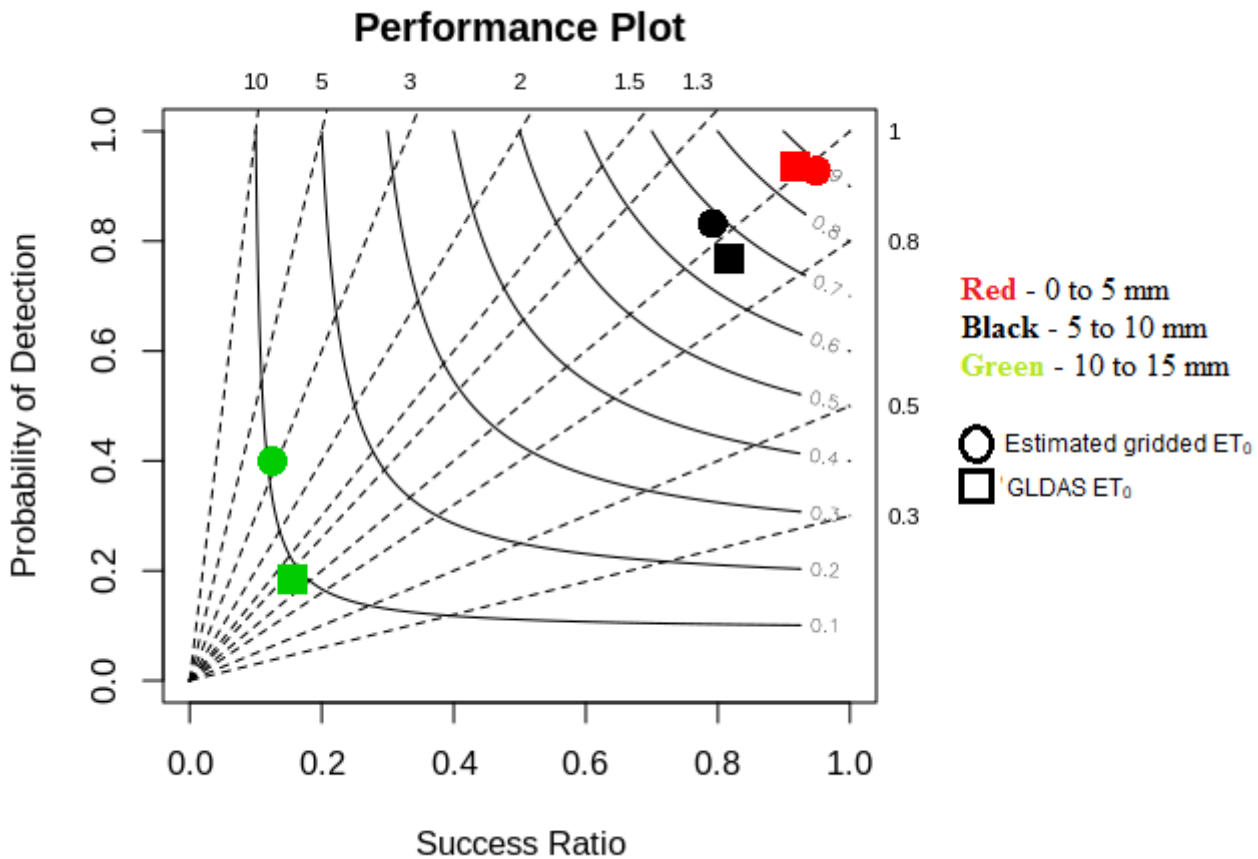


Figure 19

Performance plot of estimated gridded ET_0 and GLDAS ET_0